Urban Ecohydrology: Accounting for Sub-Grid Lateral Water and Energy Transfers in a Land Surface Model

G. Aaron Alexander[1], Carolyn B. Voter[1,2], Daniel B. Wright[1] and Steven P. Loheide II[1]

[1] Civil and Environmental Engineering - University of Wisconsin-Madison
[2] Civil and Environmental Engineering – University of Delaware

Corresponding author: G. Aaron Alexander (gaalexander3@wisc.edu)

Key Points:

- We develop an urban land surface model representation of impervious to pervious runon and canopy overhanging impervious surfaces
- Using idealized land use, we systematically examine the effects of lateral transfers on water and energy budgets over warm seasons
- We found large changes in runoff generation, water balances, and energy partitioning when lateral transfers are simulated

Abstract

Although urbanization fundamentally alters water and energy cycles, contemporary land surface models (LSMs) often do not include key urban vegetation processes that serve to transfer water and energy laterally across heterogeneous urban land types. Urban water/energy transfers occur when rainfall landing on rooftops, sidewalks, and driveways is redirected to lawns or pervious pavement and when transpiration occurs from branches overhanging impervious surfaces with the corresponding root water uptake takes place in nearby portions of yards. We introduce Noah-MP for Heterogenous Urban Environments (Noah-MP HUE), which adds sub-grid water transfers to the widely-used Noah-MP LSM. We examine how sub-grid water transfers change surface water and energy balances by systematically increasing the amount of simulated water transfer for four scenarios: tree canopy expanding over pavement (Urban Tree Expansion), tree canopy shifting over pavement (Urban Tree Shift), and directing impermeable runoff onto surrounding vegetation (Downspout Disconnection) or into an engineered pavement (Permeable Pavement). Even small percentages of sub-grid water transfer can reduce runoff and enhance evapotranspiration and deep drainage. Event-scale runoff reduction depends on storm depth, rainfall intensity, and antecedent soil moisture. Sub-grid water transfers also tend to enhance (reduce) latent (sensible) heat. Results highlight the importance not only of fine-scale heterogeneity on larger scale surface processes, but also the importance of urban management practices that enhance lateral water transfers and water storage–so-called green infrastructure–as they change land surface fluxes and, potentially, atmospheric processes. This work opens a pathway to directly integrate those practices in regional climate simulations.

1 Introduction

Urbanization creates the heterogenous patchworks of green spaces (e.g., yards, parks, street terraces) and engineered features that are central to modern life (e.g., roadways, sidewalks, buildings). Within such patchworks, green spaces differ fundamentally from engineered impervious surfaces in terms of their response to and influence on regional climate. Rain falling on vegetated surfaces typically infiltrates; a portion of this water is then returned to the atmosphere via evapotranspiration (ET). Because ET requires energy, this process creates a "sink" for incoming solar radiation that cools the surrounding environment and the overlying atmosphere. Impervious surfaces, in contrast, impede infiltration while converting incoming radiation into sensible heat that generates temperature increases. Increased runoff from impervious surfaces creates "flashy" flows that can enhance floods and impair downstream ecosystems (Hollis, 1975; Leopold, 1968; Walsh et al., 2005; Wright et al., 2012, amongst many others). Elevated sensible heat can cause Urban Heat Islands (UHI), whereby ambient temperatures in urban areas are higher than those of the surrounding region, especially during calm nighttime conditions (Oke et al., 2017). These impacts are often greatest in neighborhoods that have historically experienced practices like redlining and which remain socially and economically vulnerable today (Hoffman et al., 2020; Wilson, 2020).

Land surface models (LSMs) are one of the tools available to estimate current and future water and heat impacts in urban and other land areas. LSMs take atmospheric inputs such as precipitation, air temperature, and wind speed and simulate their effects on terrestrial water, energy, and carbon cycles (Fisher & Koven, 2020). LSMs are also critical components of the modern earth system models used to predict weather and to quantify the impacts of climate change, as feedbacks between the land surface and atmosphere can impact precipitation patterns (Barlage et al., 2021; Koster et al., 2004; Wakefield et al., 2021; Welty et al., 2020, amongst many others), near surface meteorology (e.g., Alexander et al., 2022; Berg et al., 2014; Sun et al., 2017) and hydrometeorological extremes (Lorenz et al., 2016; Miralles et al., 2019; Vogel et al., 2017). Disparity of scale is an important challenge for LSMs in earth systems models, especially when simulating built environments. Land-surface processes vary on scales of 0.1 m–1 km, but current numerical weather prediction and earth system models resolve processes on the order of 1–100 km, thus requiring substantial parametrization of sub-grid processes (Fisher & Koven, 2020; Sharma et al., 2021).

Due to the relatively coarse scales at which they are typically used, LSMs often ignore urban landscape heterogeneity. For example, the widely-used Weather Research and Forecasting (WRF) model often employs a single layer "urban canyon model." This parameterization treats all urban areas as impervious, partitioning rainfall only into runoff or evaporation from ponded water (Chen et al., 2011; Yang et al., 2015). Vegetation in the urban canyon model is either a green roof parametrization identical to the "grassland" land cover type simulated by the Unified Noah LSM, or is an averaging of outputs from X% urban and 100-X% grassland ran through the same LSM (Chen et al., 2011). These averaging methodologies can improve model skill (e.g. Vahmani & Hogue, 2015), spurring the inclusion of more specialized grid fractions and land cover classifications (e.g. Local Climate Zones described within (Fung et al., 2022) that further increase accuracy of simulated thermal resistances and aerodynamic roughness values in the Noah Multi-Physics (Noah-MP) and Unified Noah LSMs (Chen & Zonato, 2021; Mu et al., 2020; Ribeiro et

al., 2021). Nonetheless, current methodologies fail to explicitly depict ubiquitous urban hydrologic features and are unable to represent low-impact development and green infrastructure, which are increasingly used to manage urban hydrology and reduce UHIs (Avellaneda et al., 2017; Marando et al., 2022; Schwaab et al., 2021).

A potentially important omission from existing urban conceptual representations within LSMs are the lateral water and energy transfers among adjacent or overlapping land types and vegetation features. For example, urban tree canopies often overhang streets, intercepting some rainfall that would otherwise become runoff (Selbig et al., 2022). This intercepted water can evaporate, lower temperatures (Schwaab et al., 2021; Ziter et al., 2019) and modifying energy balances (Meili et al., 2021; Ryu et al., 2016; Zipper et al., 2017). Lateral transfers of water can also result from human interventions that move rainfall from impermeable surfaces to permeable surfaces. "Run-on" to an engineered permeable pavement is one such example. Such lateral transfers–below the grid scale of regional and earth systems models–can generate meaningful changes to surface runoff and urban hydrologic balances at the scale of single family homes (Voter & Loheide, 2018), city blocks (Avellaneda et al., 2017; Wang et al., 2022) and entire cities (Arjenaki et al., 2021). There are LSMs that do include urban vegetation (e.g. BEP-Tree described in (Krayenhoff et al., 2020), but these LSMs do not include the fundamental hydrology that is described above, and those models (e.g., UT&C developed in Meili et al., 2020) that do are currently not able to be directly integrated into the climate models due to their intended scale of simulation.

In this paper, we present modifications to a commonly-used LSM to explicitly represent sub-grid lateral water and energy transfers—particularly those related to vegetation—within urban environments. We combine multiple land-types to explore a range of realistic land-cover scenarios, with the goal of identifying effects of sub-grid water and energy transfers on surface water and energy balances. Specifically, we aim to answer:

1. How does the inclusion of sub-grid lateral water transfers affect runoff generation in urban environments?
2. How do lateral water transfers affect warm season distributions of deep drainage, evapotranspiration, and runoff?
3. How do changes in hydrologic fluxes link to the changes of soil moisture over the warm season?
4. How does sub-grid surface lateral water transfers change sensible and latent heat fluxes on daily and seasonal time-scales?

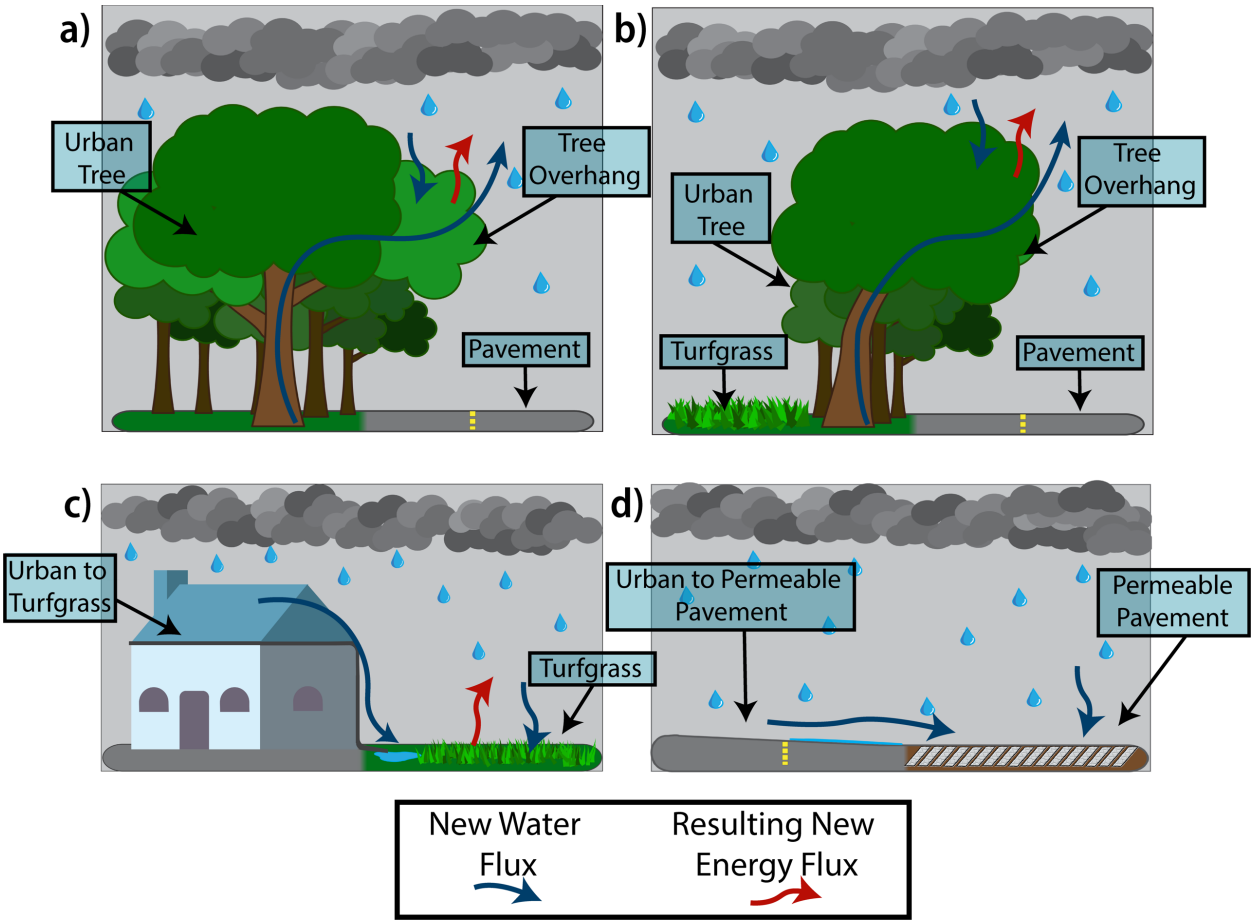

Figure 1: Conceptual diagram of new paired land types in HUE Noah-MP: Urban Tree Expansion (a), Urban Tree Shift (b), Downspout Disconnection (c), and Permeable Pavements (d). Blue arrows denote new sub-grid lateral water transfers; red arrows denote the resulting changes in energy fluxes.

2 Methods

2.1 Outline of Simulation Experiments

We were interested in systematically understanding the water and energy impacts of lateral transfers in LSMs, with a focus on three common "greening strategies" found within emerging climate mitigation plans: increasing urban tree canopy, disconnecting impervious areas, and installing pervious pavement (e.g. Milwaukee Metropolitan Sewerage District, 2013). To do this, we designed four scenario sets: two representing tree overhanging pavement (Figure 1a & 1b), one representing downspout disconnection (Fig 1c), and one representing permeable pavement (Figure 1d). Within each set, a typical case, referred to as "baseline" for each scenario, is included to represent how Noah-MP would represent our situations of interest currently. Then we integrate sub-grid water transfers between land-cover types, and incrementally increase the amount active water transfer in each scenario, using our customized LSM. How these transfers are implemented within the model is described in more detail in Section 2.2.

Tree overhanging pavement represents the lateral transfers of water due to tree canopy that extends over an impermeable surface such as a sidewalk or road, which intercepts rainfall, shades the underlying surface, and evapotranspires. While transpiration occurs across the entire footprint

of the tree's canopy, we assume that root water uptake only occurs beneath pervious areas. Within this representation, we explored two plausible situations: Urban Tree Expansion and Urban Tree Shift.

Urban Tree Expansion "grows" the tree canopy to cover more impermeable surface while maintaining the amount of tree canopy located over the permeable yard. We ran a series of simulations that varied the amount of canopy overlying the impermeable surface. The "baseline" for Urban Tree Expansion was 50% urban tree and 50% impermeable surface (i.e., no overlying canopy). Individual simulations then incremented the amount of tree canopy over pavement by 0.5% with respect to the entire simulation area, up to a maximum of 35%, meaning the other end member simulation consisted of 50% urban tree over yard, 35% urban tree over pavement, and 15% uncovered pavement.

Urban Tree Shift maintains a constant total amount of tree canopy, but places varying amounts of it over impermeable surface. To compensate for the shift of the tree canopy, a proportional amount of shallower-rooted turfgrass land cover is introduced (Figure 1). This was done to determine whether the results in Urban Tree Expansion were due to increased amount of tree canopy, or if other mechanisms were responsible for simulated changes. In the real world, Urban Tree Shift can be understood in terms of where a tree is placed within a street terrace. As with Urban Tree Expansion, the "baseline" contains 50% urban tree and 50% impermeable surface. Simulations then incremented the amount of tree canopy over pavement by 0.5%, up to a maximum of 35%. Area "uncovered" as a result of this shift was replaced with turfgrass. The end member case of Urban Tree Shift consisted of 35% turfgrass, 15% urban tree over yard, 35% urban tree over pavement, and 15% uncovered pavement.

Downspout Disconnection is a practice that eliminates the direct connection of rain gutter downspouts to impermeable surfaces like roadways or sidewalks. Instead, rainfall on rooftops is directed to surrounding vegetation—typically lawns planted with turfgrass. Simulations examining Downspout Disconnection assumed a land surface that is 30% impermeable surface and 70% turfgrass, consistent with the National Land Cover Database low-intensity urban land type, which is defined as 20%-49% impervious (Dewitz, 2021). Individual simulations then increased the amount of impermeable surface that transfers water to turfgrass from no disconnection, e.g., 0%, to full disconnection, e.g., 100%. The 0% scenario represents the "baseline" for LSMs and contains 30% impermeable surface and 70% turfgrass, with no run-on between the two. We increased the amount of disconnection by 0.5 % for each successive simulation, increasing to a total of 30% disconnection, which corresponds to fully disconnecting the impervious portion of the simulated domain.

Lastly, *Permeable Pavement* simulates flow from impervious surfaces to engineered permeable pavements, designed to infiltrate water and promote groundwater recharge, e.g., deep drainage. Permeable Pavement simulations were influenced by the guidance published by the Wisconsin Department of Natural Resources (2021), which recommends a depth of 21 inches (53 cm) and a ratio of impervious surface flowing onto permeable pavement between 4:1 and 3:1. Such guidance varies state by state, with nearby Minnesota recommending a loading ratio to not exceed 2:1 (Pollution Control Agency, 2022), North Carolina limiting loading ratios to 1:1 (Department of Environmental Quality, 2020), and Washington DC suggesting a loading ratio of 2:1 and not to

exceed a ratio of 5:1 (Department of Energy & Environment, 2019). We present simulated scenarios ranging from 100% impervious pavement to 50% impervious pavement and 50% permeable pavement (a loading ratio of 1:1). We increase the amount of Permeable Pavement from the base (0% permeable) by 1% for each successive simulation. This methodology generates high loading ratios that may be infeasible in practice due to clogging by run-on sediment, but are nonetheless useful for understanding model sensitivity**.**

In total, this experimental design yielded 254 simulation configurations across the four different scenarios: 71 Urban Tree Expansion (one baseline and 70 incrementations of 0.5% tree expansion), 71 Urban Tree Shift (one baseline and 70 incrementations of 0.5% tree shifting), 61 Downspout Disconnection (one baseline and 60 incrementations of 0.5% impervious surface disconnection), and 51 Permeable Pavement (one baseline and 50 incrementations of 1% permeable pavement). Simulations are compared throughout the text by examining end members and an intermediate simulation. For each scenario, the baseline simulation is representative of Noah-MP employing a mosaicking scheme (see Section 2.2). The most extreme end members (i.e., 35% tree overhang, 100% lateral water transfer to turfgrass, and 1:1 loading ratio of permeable pavement) were selected because they could plausibly be experienced at small scales in urban spaces, on the order of roadways and single-family homes. The intermediate simulations that are referenced throughout the text are 50% downspout disconnection, 3:1 loading ratio for the permeable pavement, and approximately the average amount of tree cover that overlaps pavement in the entire Milwaukee region based on geospatial analysis (not shown).

2.2 Description of Noah-MP HUE

Noah Multi-Physics (Noah-MP) is a LSM that describes the evolution of energy, water, and carbon cycles at the earth's surface (Niu et al., 2011). It is integrated within the WRF regional atmospheric model (Skamarock et al., 2019) and has been used in a variety of studies pertaining to land-atmosphere interactions at different scales (e.g., Alexander et al., 2022; Barlage et al., 2015, 2021). Noah-MP is also integrated into WRF-Hydro and NOAA's National Water Model for flood forecasting (Gochis et al., 2018), and has been used in uncoupled hydrologic studies (Cai et al., 2014; Lin et al., 2018; Ma et al., 2017). Noah-MP addresses shortcomings of the earlier Unified Noah (Chen et al., 1996; Ek et al., 2003) through both fundamental changes to model structure and the inclusion of multiple physics options. A major difference between Noah-MP and Noah is the treatment of vegetation; Noah-MP contains a separate vegetation canopy layer and uses an energy balance calculation method that accounts for differences between bare soil and plants, while Noah only uses an integrated surface layer. Further information on specific differences between Noah-MP and Unified Noah LSMs can be found in Niu et al. (2011). Technical aspects of Noah-MP can be found in He et al. (2023).

We have developed Noah-MP HUE: Noah-MP for Heterogenous Urban Environments. Noah-MP HUE introduces two changes: 1) a land use mosaicking scheme and 2) new "paired" urban land-types (Figure 1) with the ability to transfer water between these land-types. Mosaicking schemes are ways to represent heterogeneity by calculating weighted averages of fluxes and stores based on fractional areas within an individual LSM grid cell over different land types. They can improve the representation of the land surface (Essery et al., 2003; Fisher & Koven, 2020; Li et al., 2013). The mosaic scheme we implemented in Noah-MP HUE follows the one previously implemented in the Unified Noah model by Li et al. (2013).

We now outline the three new paired land cover types, which include a total of six new land categories that transfer water within Noah-MP HUE. The first two paired land cover types represent tree cover that overhangs pavement, which intercepts rainfall proportional to the overlying Leaf Area Index (LAI), like all other vegetated land types in Noah-MP. Rainfall that is not intercepted by tree canopy becomes runoff, exactly like the impervious surfaces in Noah-MP. Tree canopy located over pavement transpires by extracting water from the soil zone beneath the adjacent pervious area where the urban tree is planted—not the soil zone under the pavement—by first calculating a soil transpiration reduction factor–a simplified Feddes Function common in LSMs–based on available soil moisture (Feddes et al., 1976; Niu et al., 2011). Root water uptake is calculated as shown in Equation 1:

$$\boldsymbol{RWU_{i_{Total}} = \chi_i \cdot T_{Tree\ over\ Yard} \cdot \beta_i + \frac{A_{Tree\ Over\ Pavement}}{A_{Tree\ over\ Yard}} \cdot \chi_i \cdot T_{Tree\ over\ Pavement} \cdot \beta_i} \quad \textbf{(1)}$$

Where $\boldsymbol{i}$ denotes Noah-MP's different soil layers (typically four), $RWU_{i_{Total}}$ is the rate of root water uptake that accounts for both the Urban Tree over Yard and the Urban Tree over Pavement distributed across soil layers in Noah-MP HUE, β_i is the unitless soil transpiration reduction factor that is calculated for the soil layers in the yard, $T_{Tree\ over\ Yard}$ is potential transpiration rate of Urban Tree over Yard, $T_{Tree\ over\ Pavement}$ is the same for Urban Tree over Pavement, $\boldsymbol{A_{Tree\ Over\ Pavement}}$ is the normalized area of the Tree over Pavement in a grid cell, $\boldsymbol{A_{Tree\ over\ Yard}}$ is the same but for the Tree Over Yard,. Within Noah-MP, $\boldsymbol{\chi_i}$ acts as root indicator function, assuming a value of one if roots are present or zero if there are no roots present in a given soil layer, though is conceptually similar to the root distribution functions in more complex LSMs (Gale & Grigal, 1987; K. Oleson et al., 2013; Zeng, 2001). Even though the tree canopy extends over the pavement, we assume that roots (and root water uptake) occurs only from permeable areas underneath the footprint of the canopy; thus transpiration from the Tree over Pavement is scaled by the relative ratio of the Urban Tree over Pavement and the Urban Tree over Yard areas and added to the RWU term of the yard. This methodology is agnostic to the multiple vegetation physics options within Noah-MP.

The second new paired land cover type—Downspout Disconnection—moves water laterally from an impervious surface to turfgrass. We developed an urban turfgrass land cover that uses parameters based on those presented in Voter & Loheide (2018), with the additional required parameters coming from the grassland land cover type already in Noah-MP and literature**.** Table S1 in supplementary material gives turfgrass parameter values that are not defaults from Noah-MP grassland (Niu et al., 2011). Runoff generated by impervious surfaces is redirected to turfgrass at each time step within the model. This process is governed Equation 2:

$$\boldsymbol{W = P + \frac{A_{Impervious}}{A_{Recieve}} \cdot R_{Impervious}} \quad \textbf{(2)}$$

Where W denotes the combined depth of water reaching the land surface, $\boldsymbol{P}$ is the depth of precipitation incident to turfgrass, $A_{Impervious}$ is the normalized area of the impervious surface that has water routed to a pervious surface, $A_{Recieve}$ is the same normalized area but for the permeable surface that will receive the water, and $R_{Impervious}$ is the depth of runoff generated by the laterally connected impervious surface. $R_{Impervious}$ is scaled by the ratio of the impervious surface area and the receiving land area in order to appropriately scale the depth of run-on received by the turfgrass. The final paired land cover type—impervious surface laterally transferring water

to permeable pavement—is also governed by Equation 2, with permeable pavement receiving water instead of turfgrass.

2.3 Study Location and Model Configuration

All simulations are forced using hourly meteorological inputs of precipitation, temperature, wind speed, humidity, and radiation from the North American Land Data Assimilation System version 2 (NASA, 2015) centered on Milwaukee, Wisconsin (43.04°N, 87.91°W). Simulations were carried out at a 5-minute timestep for integration and output for three continuous years, 2018 to 2020, and all analyses focused on warm seasons, defined as 1 May to 1 November. Each simulation started on 1 April 2018 and utilized the first month (until 1 May 2018) as spin-up. The three simulated years had warm season rainfall depths of 841 mm in 2018, 809 mm in 2019, and 648 mm in 2020–substantially higher than the average of 533 mm in the region over the past 30 years but consistent with the recent increases in precipitation associated with climate warming. Each simulation represents a location that has multiple interacting land covers but no defined spatial resolution. Instead, the wide range of these multiple land cover fractions tested within our experimental design were chosen to give insights into a) the variability of land cover fractions that might exist in different locations across an urban area, or b) the variability of land cover fractions that might result when land use data are aggregated to spatial resolutions. In a spatially distributed modeling approach like that used in typical Noah-MP simulations, the percent land type composition for each grid cell would be determined from detailed land cover maps for the area of interest.

We used soil hydraulic properties representative of silt loam and assumed initially saturated soil conditions, 0.476 m^3 m^{-3} for all land types except for the Permeable Pavement. This is reasonable, as spring snowmelt brings soils to saturation in the region. The top two soil layers of Permeable Pavement used a modified sand soil classification to achieve an infiltration rate between 10 in hr^{-1} and 100 in hr^{-1}, in line with the requirements from the Wisconsin Department of Natural Resources (2021). To achieve the desired infiltration rate of 360 mm/hr, we set the saturated hydraulic conductivity as $1.76 \cdot 10^{-4}$ m s^{-1}, and set all other soil characteristics to those typical of sand (provide ref for the values, here and above for the silt loam) The bottom two soil layers of the permeable pavement are parameterized as the aforementioned silt loam soil texture class.

In terms of model physics parameterization, we used approaches that have been previously recommended for non-atmospherically coupled Noah-MP simulations (He et al., 2021). These options include using table-specified vegetation fractions and interpolated monthly LAI (i.e., no dynamic vegetation model or crop model), the Ball-Berry formulation for canopy stomatal resistances, the CLM formulation for soil transpiration reduction factor (Niu et al., 2011), the original Unified Noah surface and subsurface runoff (He et al., 2023; Schaake et al., 1996), the Monin Obukov similarity theory solver for surface layer coefficients (Brutsaert, 1982), linear effects of frozen soil on permeability, direct solving of supercooled liquid water within the soil (Niu & Yang, 2006), the CLASS formulation for dynamic ground snow surface albedo (Verseghy, 2007), the Jordan approach for partitioning precipitation into rainfall or snowfall (Verseghy, 2007), a semi-implicit flux top boundary condition for top layer soil temperature, and the Sakaguchi & Zeng (2009) approach for surface resistance to evaporation and sublimation. All simulations used default parameters in the Noah-MP unless otherwise specified (He et al., 2023; Niu et al., 2011). This study uses the bulk urban treatment instead of any explicit urban physics model like the urban

canyon (Kusaka et al., 2001) or BEP (Martilli et al., 2002) models, and utilizes the default bulk thermal and radiative properties for pavements.

3 Results

3.1 Event Scale Surface Runoff Generation

Lateral surface water transfers reduce event scale runoff across all scenarios when compared to that generated by the baseline LSM (Figure 2). The magnitude of runoff reduction varies based on the type and amount of transfer. For example, the baseline LSM simulations of the largest storm in our analysis–a storm depth of 130 mm–generated 72 mm of runoff for tree scenarios, 51 mm for non-disconnected downspout, and 130 mm for impervious pavements. For this same storm, runoff totals were 66 mm for Urban Tree Expansion (35% canopy over pavement), 68 mm for Urban Tree Shift (35% canopy over pavement), 30 mm for Downspout Disconnection (100% disconnection), and 71 mm for Permeable Pavement (75% traditional pavement running onto 25% permeable pavement). These correspond to a runoff reduction associated with lateral transfers ranging from 6% (Urban Tree Shift) to 45% (Permeable Pavement). Downspout Disconnection and Permeable Pavement reduce runoff more than the urban tree scenarios.

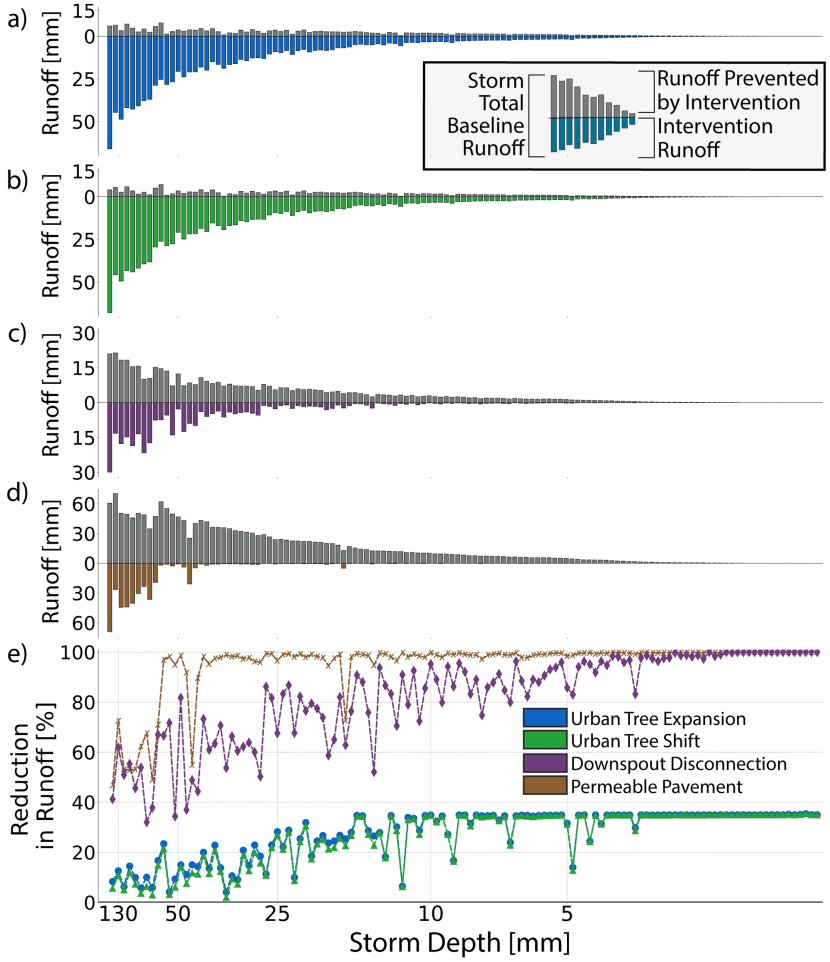

Figure 2: Warm season event-scale runoff ordered by storm depth Urban Tree Expansion (a), Urban Tree Shift (b), Downspout Disconnection (c), and Permeable Pavement (d) in Milwaukee, WI. Colored bars below the x-axis are the amount of runoff generated with lateral transfers using Noah-MP HUE, while grey bars indicated additional runoff with no lateral transfers. Breakdowns

of land cover are 35% canopy over pavement for both tree scenarios, 100% downspout disconnection (e.g., 30% roof pavement transferring water to an adjacent 70% turfgrass), and 75% traditional pavement running onto 25% permeable pavement. Percentage differences between the typical LSM representation (i.e., Noah-MP) and Noah-MP HUE representations are also provided (e). Storm events, e.g., each bar, are defined by a dry period of at least 12 hours.

The extent of runoff reduction varies with storm depth, though not monotonically. While runoff reduction generally increases as storm depth decreases, this trend is punctuated by storms with similar depths but vastly different runoff reductions (Figure 2d). This variability is likely due to effects of antecedent soil moisture and within-storm rainfall temporal variability. For example, the minimum runoff reduction relative to rainfall depth due to sub-grid lateral transfers is not during largest storm (rainfall depth of 130 mm) for interventions other than Permeable Pavement, but instead the 21st largest storm (rainfall depth of 36 mm) for both Urban Tree Expansion and Urban Tree Shift, and the 7th largest storm (rainfall depth of 73 mm) for Downspout Disconnection (Figure 2e). The 21st largest storm was characterized by light rainfall in the mid-summer over dry soil conditions, while the 7th largest storm included a pulse of heavy rainfall–30 mm hr^{-1}–which likely overwhelmed soil infiltration capacity. Complete reduction of runoff does occur for Permeable Pavements (below 18 mm storm depth) and Downspout Disconnection (below 2 mm), but never occurs for either urban tree scenario, which cap at 35% runoff reduction because of the existence of uncovered pavement in the baseline LSM.

3.2 Seasonal Water Fluxes

Lateral water transfers impact warm season hydrology by changing the partitioning of rainfall into surface runoff, evapotranspiration (ET), soil moisture storage, and deep drainage. Deep drainage is water that makes it through the first two meters of the soil column and could become groundwater recharge and is sometimes referred to as subsurface runoff in other LSMs. Figure 3 and Figure **4** provide breakdowns of average warm season fluxes for all simulations. We provide a graphical summary of changes for selected scenarios in Figure S1 of supplementary material for each simulation set.

Urban Tree Expansion increases ET and decreases runoff and deep drainage (Figure 3a). Runoff decreases range from 1 to 64 mm in total, but only a small fraction—0.1 to 3.8 mm—of the observed decrease comes from vegetated surfaces. Thus, even as the canopy expands in simulations, runoff is generated (95% on average) primarily over paved areas. ET increases range between 0.1% and 16% relative to rainfall, but there are opposing trends if the ET occurs over a vegetated surface or pavement: ET from a paved area increases from 0 to 160 mm–a 20% increase relative to precipitation–by adding 35% overhanging canopy. Simultaneously, ET decreases from 376 mm to 340 mm over vegetated surfaces–a decrease of 4% relative to precipitation, driven by drier soils, which hold between 0.1% to 6% less water over the growing seasons. Deep drainage decreases between 0.3% and 1.3%. In short, the Urban Tree Expansion scenario increases root water uptake and ET, causing a reduction in soil moisture and deep drainage, while runoff reduction is mostly driven by intercepting rainfall by the new, overlying tree canopy (Figure 3a).

Compared to Urban Tree Expansion, Urban Tree Shift causes smaller decreases in runoff and creates smaller, non-linear changes in both ET and deep drainage (Figure 3b). Runoff generation over the paved portion for this case is identical to those in Urban Tree Expansion. Runoff

388 generation over vegetated surfaces is larger, however: 25 mm in the most extreme case. ET
389 increases until 29% of the domain is tree canopy shifted over pavement, releasing 440 mm over
390 the warm season, but then decreases to 437 mm for the 35% shifted tree end member. In contrast
391 with Urban Tree Expansion, deep drainage now increases by 2% compared to baseline. Soil
392 moisture deficit mirrors the behavior of ET, increasing until 25% of the simulated domain is tree
393 canopy over pavement – achieving a deficit of 61 mm – and then decreases. Changes in soil water
394 fluxes in Urban Tree Shift scenarios are associated with the replacement of deep-rooted tree
395 landcover with a shallow-rooted turfgrass (200 cm vs. 30 cm rooting depth), resulting in the areal
396 extent of the tree roots decreasing, drying out the tree portion of the domain and causing simulated
397 ET to decrease due to lack of available soil water. While parts of the domain are drier, the overall
398 domain is moister compared to the baseline LSM, causing greater runoff in vegetated portions.
399
400 Downspout Disconnection (Figure 4a) decreases runoff, slightly increases ET, and markedly
401 increases deep drainage. Seasonal runoff reduction ranges from 0.4% to 22% relative to the
402 baseline, despite runoff generated by turfgrass increasing as more water is added to the vegetated
403 portion of the domain due to the disconnection intervention. ET increases up to 27 mm as
404 simulations transition from no downspout disconnection to full disconnection. Virtually no water
405 stress occurs, meaning depleted soil moisture from root water uptake in the upper 30 cm of the soil
406 column is readily replenished by frequent rainfall. As a result, rainfall, enhanced by run-on from
407 adjacent pavement, is preferentially partitioned into deep drainage, which increases from 67 to 187
408 mm. Finally, soil moisture deficit decreases slightly due to increased run-on compared to the
409 baseline LSM case, by roughly 2% on average.
410
411 Permeable Pavement interventions reduce runoff and funnel this water into deep drainage
412 (Figure 4b). A small increase in permeable pavement can lead to large water balance changes. By
413 increasing the amount of permeable pavement from none to 5% of the simulated domain, surface
414 runoff is reduced by 24%. By further increasing to 10% permeable pavement, runoff is reduced by
415 44%. Soil moisture storage also decreases slightly–a maximum of 3% of the average warm season
416 rainfall–though the decrease is due to rainfall depths becoming less likely to fill available soil
417 water storage.

418

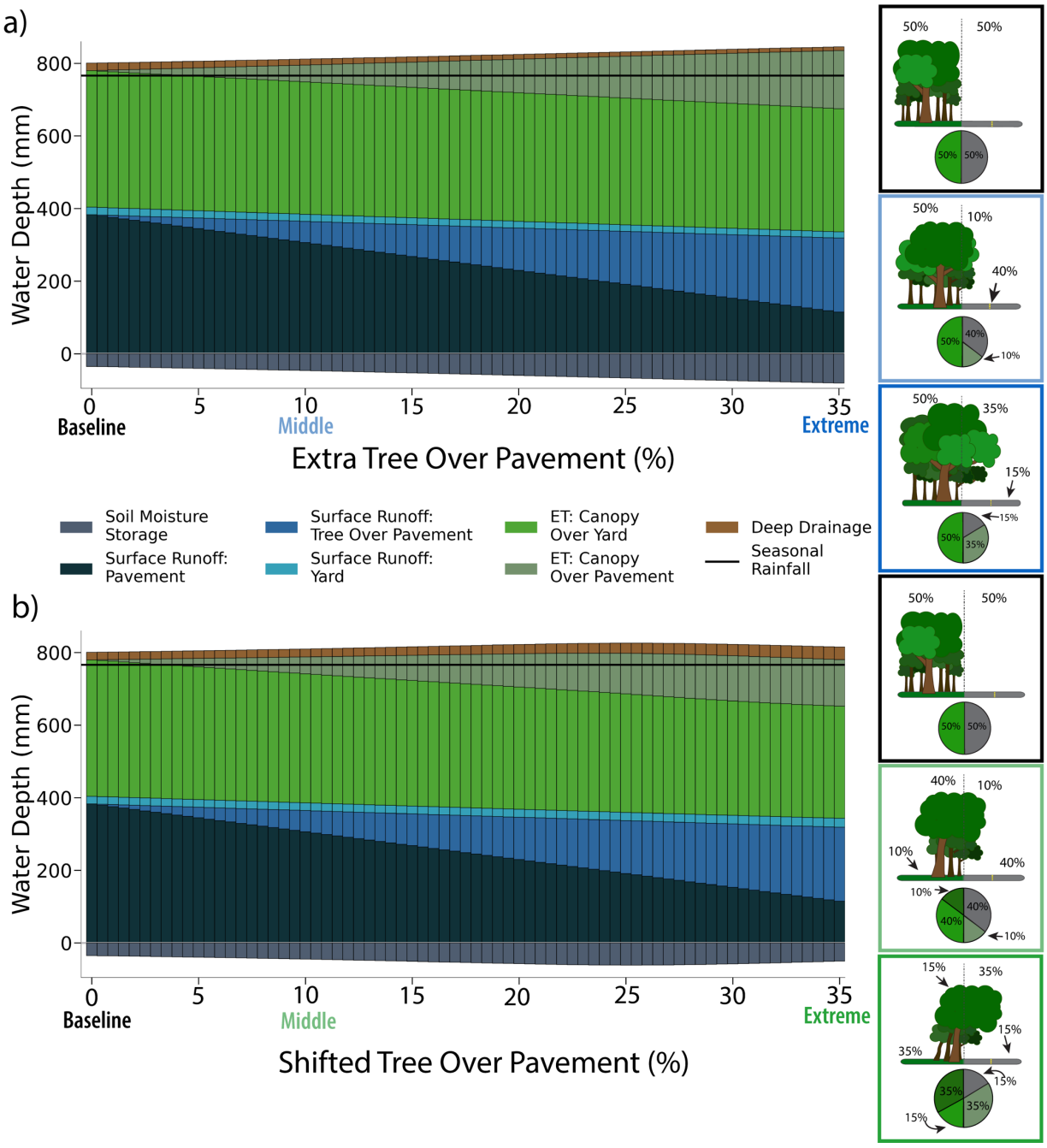

419

420 **Figure 3**: Change in the partitioning of rainfall (mm) to different water fluxes over a suite of Urban
421 Tree Expansion (a) and Urban Tree Shift (b) averaged over three warm seasons from Noah-MP
422 HUE. Average seasonal rainfall is shown by the solid black line, while the zero line is denoted in
423 solid grey. Icons depict different key scenarios' flux volume breakdown.

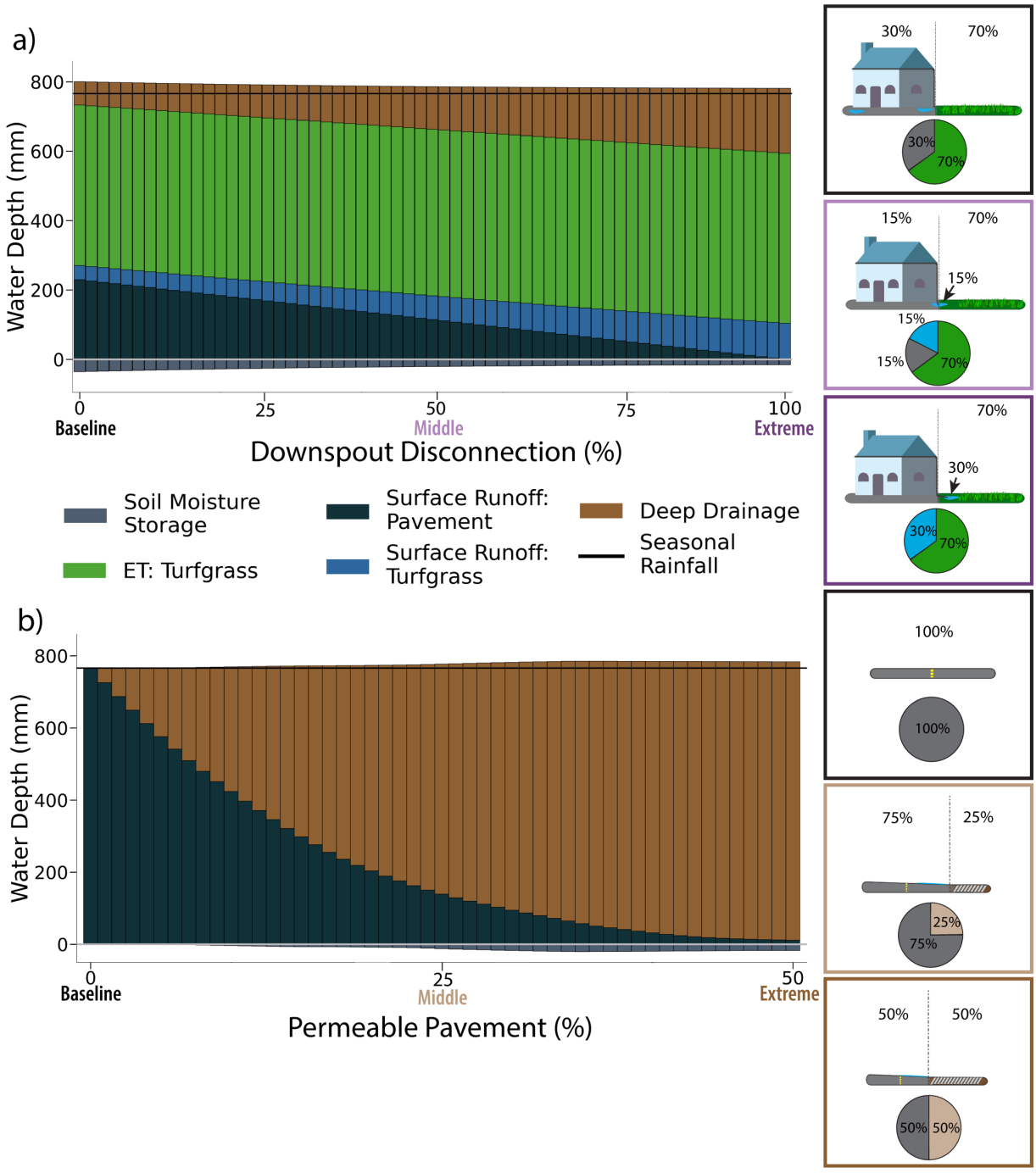

Figure 4: As in Figure 3, but for Downspout Disconnection (a) and Permeable Pavement (b) simulations. Note that "Surface Runoff: Pavement" (dark blue) in panel b is from rainfall that was first laterally transferred from impermeable pavement to the permeable pavement and not subsequently infiltrated.

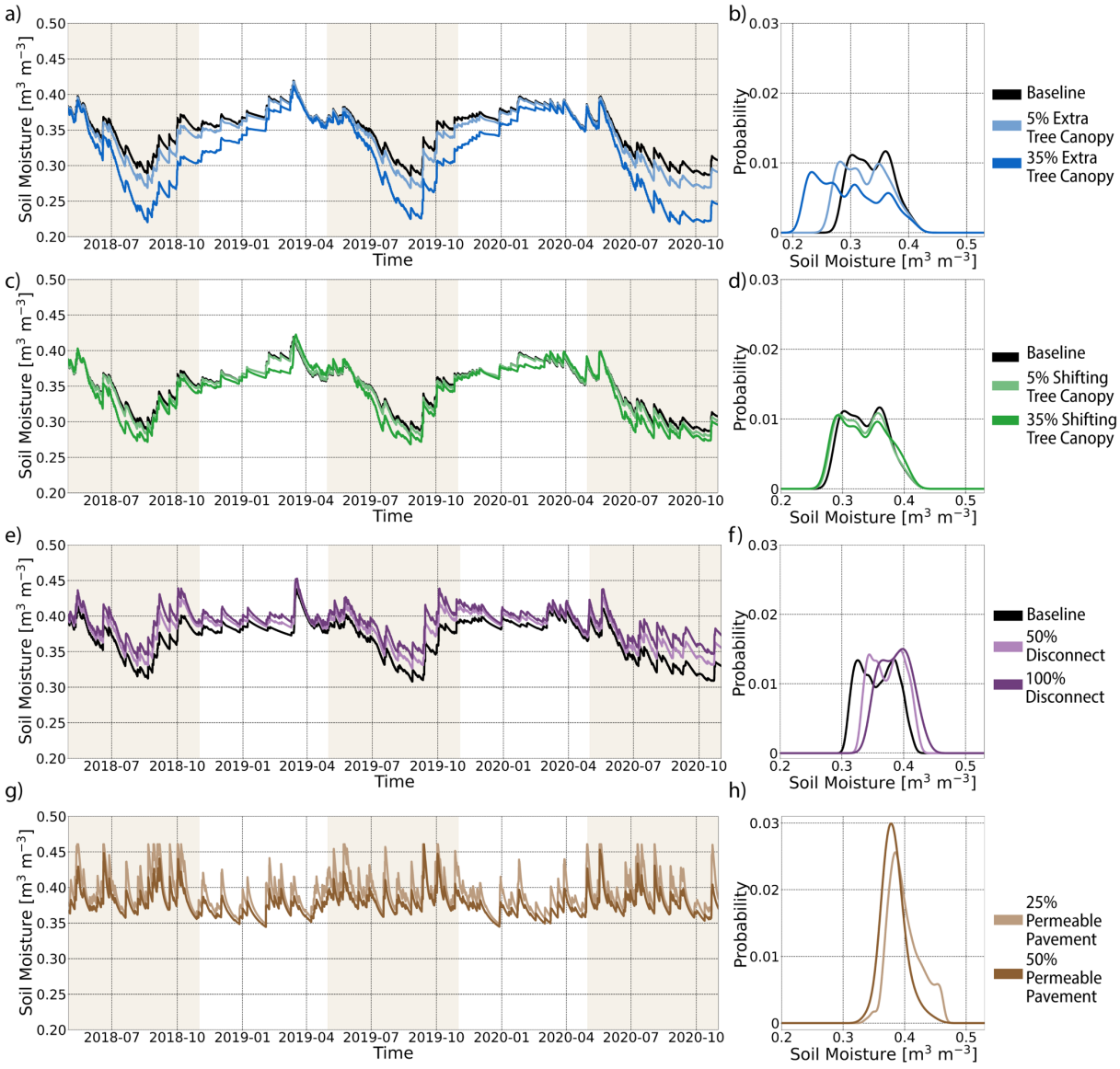

Figure 5: Total column-averaged soil moisture time series of the pervious portion of the domain (e.g., soil moisture under vegetation or pervious pavement) for Urban Tree Expansion (a), Urban Tree Shift (c), Downspout Disconnection (e), and Permeable Pavement (g) for different scenarios. Warm seasons are shaded in panels. Empirical PDFs estimated from all three simulated warm seasons shown for Urban Tree Expansion (b), Urban Tree Shift (d), Downspout Disconnection (f), and Permeable Pavement (h). No baseline simulation is plotted for Permeable Pavement, as typical pavement does not change soil moisture.

438
439 **3.3 Seasonal Soil Moisture**
440 Time series of total soil column (200 cm) soil moisture (SM) in the vegetated/permeable parts
441 of simulations, when paired with empirical probability density functions (PDFs), give insight as to
442 why changes in runoff, deep drainage, and ET occur throughout the warm season (Figure 5).
443
444 Urban Tree Expansion, which decreased runoff and deep drainage and increased ET, tended to
445 dry SM throughout the column. The magnitude of changes varied greatly with the amount of extra
446 canopy present in simulations (Figure 5a). SM stress begins at 0.25 m^3 m^{-3} for the silt loam soil
447 class and chosen parameter scheme. During Urban Tree Expansion (Figure 5a & b), SM stress is
448 common in simulations with more tree canopy over pavement and shifts simulated SM PDFs to
449 the left (Figure 5b), especially during the height of the warm season due to increased canopy ET.
450 The overall drier soils lead to enhanced infiltration, but less soil water goes to deep drainage, due
451 to the enhancement of ET.
452
453 Urban Tree Shift decreased runoff and increased both deep drainage and ET, resulting in
454 slightly lower SM compared to the baseline simulation (Figure 5c). SM stress is more subtle in the
455 Urban Tree Shift scenario, as the soil column does not dry below 0.25 m^3 m^{-3}, seemingly avoiding
456 soil water stress (Figure 5c & d). However, by examining separately the turfgrass and urban tree
457 components of the vegetated portion of the domain, one finds that the column of the urban tree
458 SM drops below this soil stress threshold (not shown) when 28.5% or more of the tree canopy is
459 located over pavement, limiting ET in more extreme simulations. SM PDFs from the Urban Tree
460 Shift simulations "flatten out" by both moving slightly to the left, signaling drying of the soil under
461 urban tree, and slightly right, signaling moister soil-under-turfgrass conditions compared to the
462 baseline (Figure 5d). The slight shift right is likely due to wetting fronts more readily moving past
463 shallow-rooted turfgrass, which is a key reason for the dramatic increase in deep drainage in this
464 scenario.
465
466 Downspout Disconnection results in a net increase in SM, shifting the time series upward
467 (Figure 5e) and pushing the PDF to the right (Figure 5f) as the degree of disconnection is increased.
468 Routing rooftop water to the yard through downspouts makes available water for infiltration,
469 generating an increase of SM throughout the soil column in the yard and ultimately resulting in
470 increased deep drainage. Higher SM also reduces infiltration capacity and increases the likelihood
471 of runoff generation, though not enough to match runoff from the baseline LSM with no
472 disconnection (Figure 4).
473
474 Permeable Pavement integration opens a new pathway for urban rainfall to infiltrate, leading to
475 increases in deep drainage. More permeable pavement leads to a decrease in the permeable
476 pavement SM throughout the column as the engineered soil beneath the permeable pavement
477 drains very efficiently (Figure 5g & h). In the selected time series (Figure 5g), the SM of the 25%
478 permeable pavement simulation reaches saturation during some rainfall events, indicating
479 precipitation plus run-on exceeds infiltration capacity; note that this does not occur in the 50%

permeable pavement simulation, which indicates that scenario could have accommodated more rainfall.

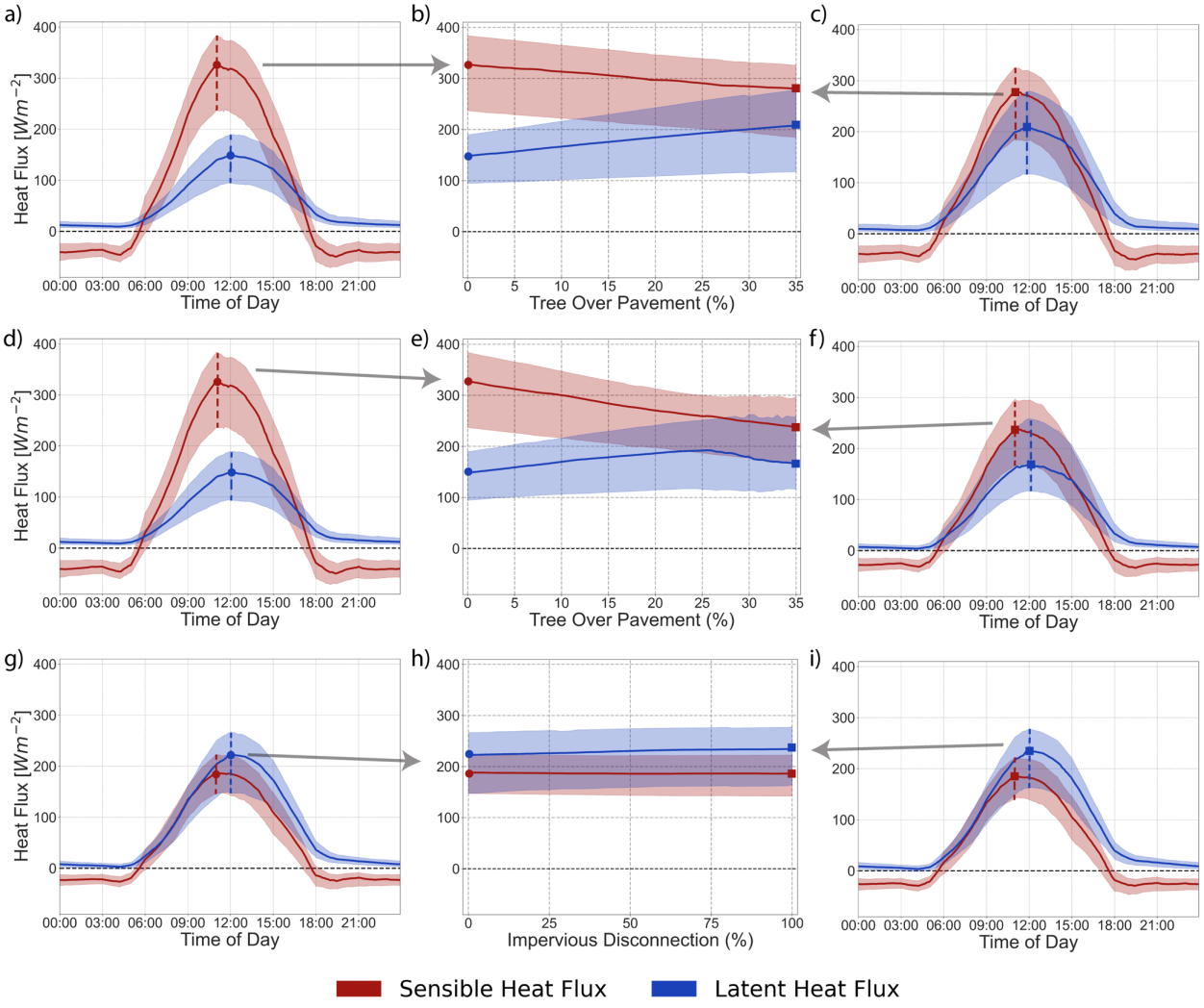

Figure 6: Median diurnal patterns (solid lines) and interquartile ranges (shaded areas) for sensible (red) and latent heat (blue) fluxes for Urban Tree Expansion (a and c), Urban Tree Shift (d and f), and Downspout Disconnection (g and i). Leftmost column depicts "Baseline" simulations, while the rightmost column depicts "Extreme" simulations (e.g., most canopy over pavement or full downspout disconnection). Middle column (b, e, h) show median diurnal maximum heat flux and interquartile range across all simulations. Circles correspond to the leftmost column's maxima, while squares correspond to extreme simulations' maxima from the rightmost column.

3.4 Diurnal Energy Evolution

Lateral water transfers not only affect water fluxes but also lead to increases in daily latent heat (LE) and decreases in sensible heat (H). We aggregated sensible and latent heat fluxes by time of day and found the median, thus estimating typical diurnal patterns, with uncertainty bounds of the

494 25% and 75% (i.e., the interquartile diurnal pattern; Figure 6). We do not report changes in
495 Permeable Pavement (maximum difference of 0.01% across simulations).
496
497 The magnitude and mechanisms of change in diurnal energy evolution differs dramatically
498 between scenarios. Urban Tree Expansion peak LE ranges by 60 W m^{-2} between baseline and 35%
499 canopy scenarios (Figure 6b), but are smaller for Urban Tree Shift with a range of 20 W m^{-2} (Figure
500 6e). In the case of Urban Tree Expansion, LE changes are directly linked to the larger tree canopy
501 area increasing the transpiring footprint. Urban Tree Shift changes are nonlinear: LE increases
502 until 26% of the domain contains tree over pavement, and then decreases, Finally, Downspout
503 Disconnection increases peak LE by 11 W m^{-2} by increasing available water and has negligible
504 impact on H (2 W m^{-2}). Outside of arid or semi-arid climates, we would not expect major changes
505 in LE and H due to more available soil water, as increased soil water does not enhance LE at the
506 expense of H during the daytime unless drought conditions occur (Miller et al., 2020; Shields &
507 Tague, 2015; Voter & Loheide, 2021).
508
509 Urban Tree Expansion and Urban Tree Shift both reduce H during the daytime, with this change
510 relating to both increased ET and changes in effective surface thermal properties. The most marked
511 change occurs near midday, when peak H reduces by 47 W m^{-2} for Urban Tree Expansion (Figure
512 6b) and 89 W m^{-2} for Urban Tree Shift (Figure 6e). Most of this reduction is likely due to more
513 energy partitioning to LE, though hints of another mechanism of H reduction—changing the
514 effective emissivity and albedo in simulations—lie in the variability (shading in Figure 6). H
515 variability in Urban Tree Expansion and Urban Tree Shift remain nearly constant at the daily scale
516 across simulations, but LE becomes more variable. Tree canopy shades the pavement in both
517 Urban Tree Expansion and Urban Tree Shift, resulting in peak H reductions with a nearly constant
518 interquartile range. At the same time, more of the tree canopy is over a warmer surface (pavement
519 surface temperatures are warmer than the vegetated surface by an average of 2 K during the
520 daytime), which induces more variable LE (a widening of the interquartile range shading).
521
522 **3.5 Warm Season Energy Balances**

523 Diurnal energy balances and environmental factors like rainfall depth and time between rain
524 events change seasonal LE/ET and H patterns, especially when vegetation is water limited. We
525 investigate changes in warm season scale energy patterns and their links to sub-grid lateral water
526 transfers by examining total daily LE (Figure 7) and H (Figure 8) across every simulation for the
527 2019 warm season. Results for 2018 and 2020 warm seasons are provided in Figures S5 – S8 in
528 Supplemental Material.
529
530 Urban Tree Expansion, Urban Tree Shift, and Downspout disconnection all convert more
531 available radiation (net radiation minus ground heat flux storage) into LE during the warm season
532 when more sub-grid lateral water transfer is included (Figure 7). This corresponds to a reduction
533 in seasonal H totals (Figure 8). All scenarios show "banding" of higher-than-average (lower than
534 average) LE (H) days during and directly after days with rainfall, representing the effects of
535 enhanced infiltration and interception on energy partitioning. In Urban Tree Expansion (Figure 7a
536 & b, Figure 8a & b) and Downspout Disconnection (Figure 7e & f, Figure 8e & f) increases LE
537 and corresponds to nearly identical decreases H as sub-grid lateral water transfer increases. In the
538 Urban Tree Shift scenario, however, a drying effect occurs in which LE suddenly drops when 25%
539 or more of the simulated area is tree over pavement (Figure 7c). This drying creeps earlier into the

warm season as tree over pavement fraction increases, coincident with earlier onset of soil water stress. Though there is a large reduction in LE due to drying–on the order of 2 GJ in some extreme cases–the same magnitude of increase in H is not observed, tied to changes induced by modified radiative and thermal properties like albedo, emissivity, and heat capacity.

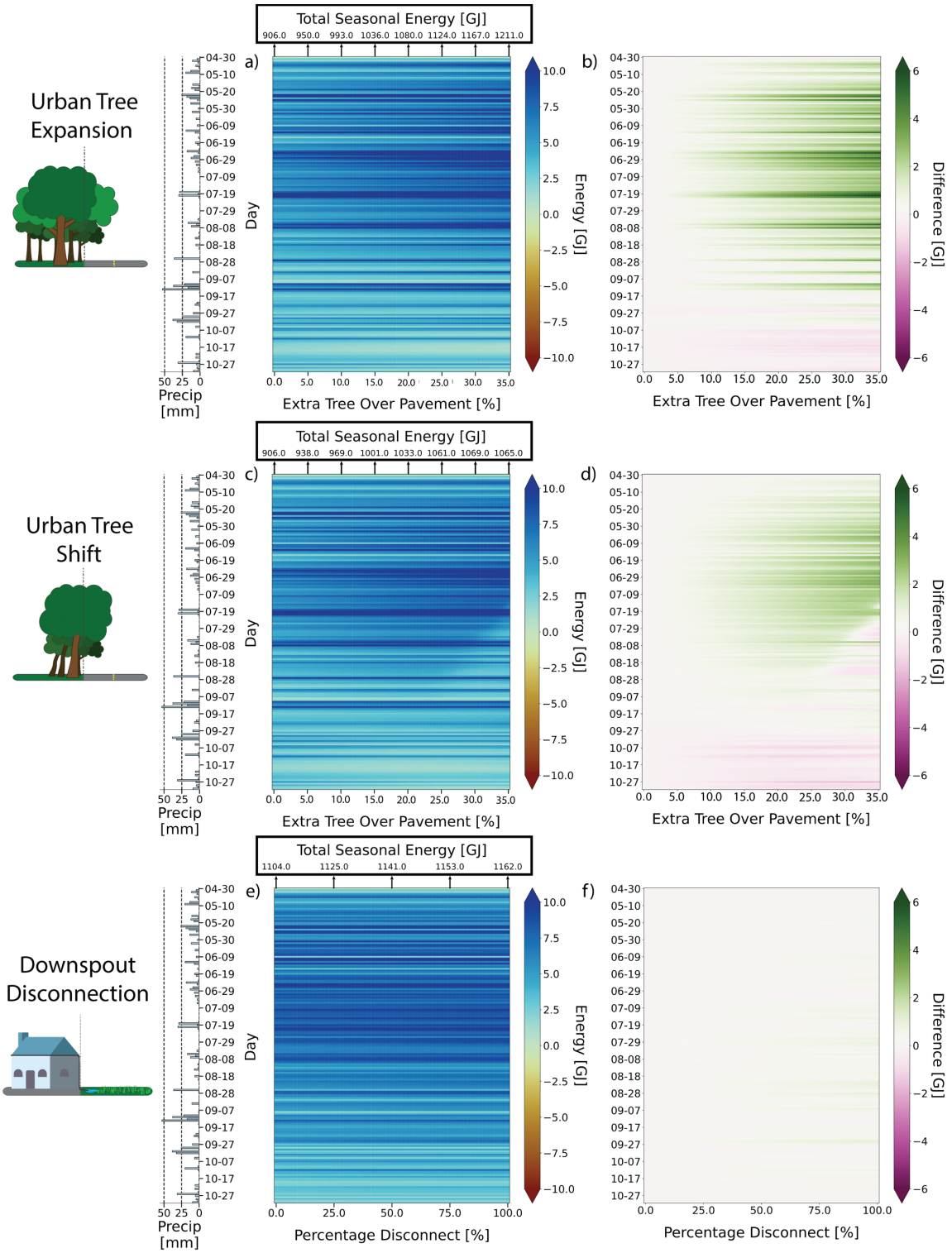

Figure 7: Daily integrated LE from the entire simulated domain over the 2019 warm season and difference from baseline heatmaps, both in GJ. Within heatmaps, rows are individual days and columns are the different simulated scenarios. Panels a) and b) are Urban Tree Expansion simulations, Panels c) and d) are Urban Tree Shift, and Panels e) and f) are Downspout

549 Disconnection. A hyetograph of daily precipitation on the left and select integrated total energy on
550 the top of each heatmap is provided for reference.

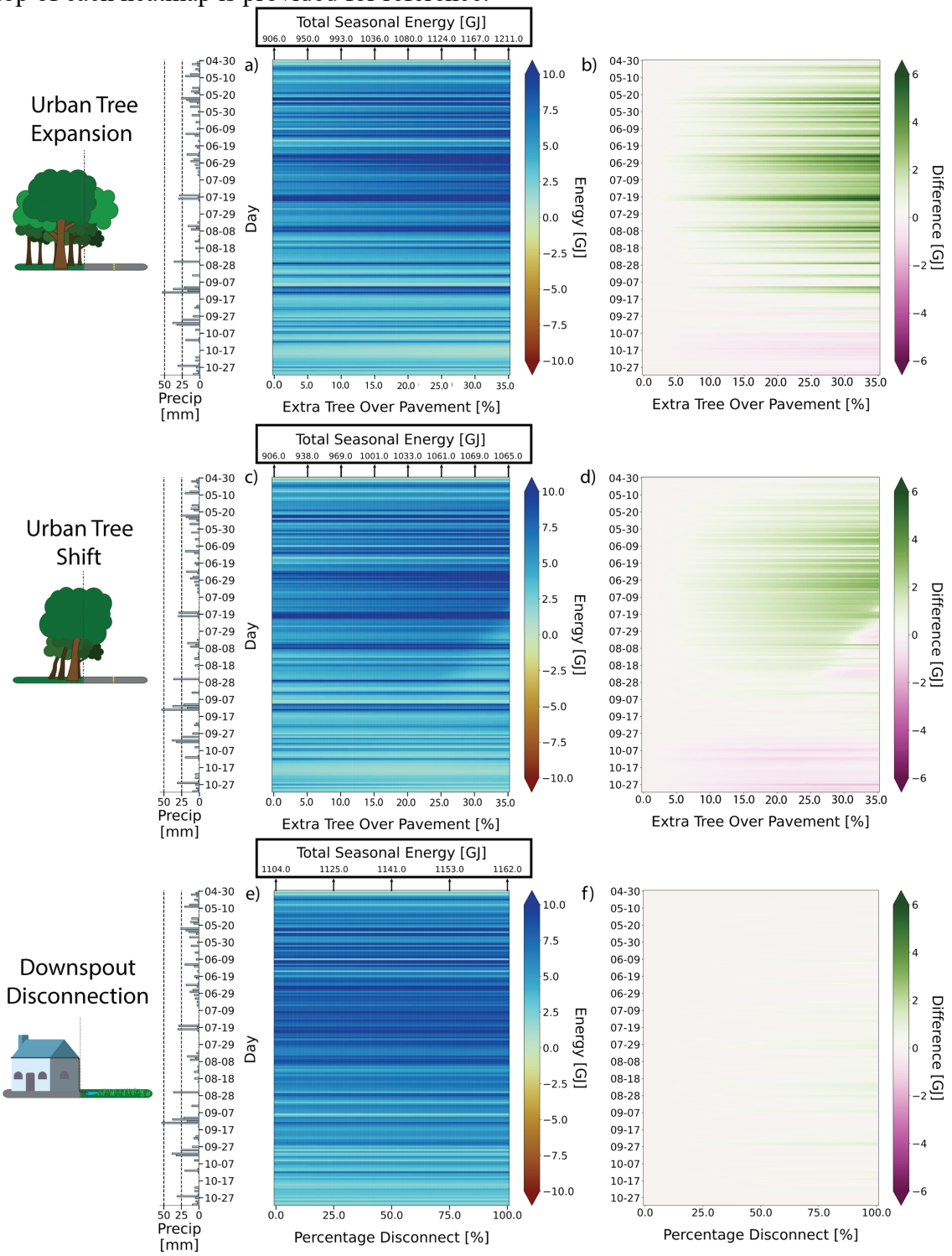

551
552 **Figure 8**: As in Figure 7, but for H.

553
554

555 **4 Discussion**

556 **4.1 Implications for Land Surface Modeling in Urban Regions**

557 Current LSM frameworks are not generally able to represent the highly heterogenous
558 hydrologic processes that exist in urban environments. The usage of a single dominant land type
559 (or even a mosaic of land types within a single grid) that do not interact with other surface types
560 is not supported by recent work showing the impact of lateral transfers on the water balances of
561 single home parcels (Voter & Loheide, 2018), city blocks (Avellaneda et al., 2017; Wang et al.,
562 2022), and city-scale responses of runoff and storm water systems (Arjenaki et al., 2021). LSMs
563 are somewhat distinct from models developed for purely hydrologic prediction, in that they
564 primarily aim to provide boundary conditions for coupled atmospheric models. The increasing
565 complexity and resolution of atmospheric models, however, has driven LSM development to
566 include more processes from other scientific disciplines (Fisher & Koven, 2020). The need to
567 correctly quantify the urban energy balance–even in relatively coarse atmospheric and earth
568 system simulations–requires the inclusion of these complex, fine-scale lateral water transfers, since
569 they directly impact water and energy cycling at multiple scales (Oke et al., 2017). Our results
570 indicate that current LSMs that neglect lateral water transfers generally create too much runoff and
571 too little ET in urban areas, which could affect simulated atmospheric processes and their impacts.
572 Noah-MP HUE presents a first step in bridging this gap by adding new physics that allows for sub-
573 grid sharing of water and energy.
574
575 The scale at which we would expect to see certain results is important to understand when using
576 an LSM like Noah-MP. This model is intended to be used for applications that span in scale from
577 continental simulations of atmospheric processes down simulations of a handful of watersheds
578 (Barlage et al. 2021, Lin et al. 2018, amongst many others). As explained in Section 2.3,
579 simulations presented in this study are representative of probable distributions of land-cover
580 interactions in a city aggregated at different scales (i.e., to different grid resolutions). For example,
581 at a small scale, e.g., the street in front of a single household, we might find that 35% of pavement
582 is covered by tree canopy, which is the end member scenario in both Urban Tree Expansion and
583 Urban Tree Shift. If we increase the scale to capture an entire neighborhood, we would likely find
584 smaller fractions of pavement covered by trees. Similarly, in Downspout Disconnection and
585 Permeable Pavement scenarios, larger fractions of disconnection correspond with smaller scales
586 of interest (e.g., a single house or street). Adding further complexity to Downspout Disconnection
587 and Permeable Pavement scenarios is the fact that they are determined by ordinances in a region
588 of interest, and thus require care when integrated at larger scales to ensure realistic loading ratios
589 are preserved.
590
591 The changes brought by sub-grid lateral water transfers in urban regions are complex and
592 provide nuanced results that would be missed without explicit integration into a physically-based
593 model. Adding lateral water transfer in Urban Tree Expansion and Urban Tree Shift scenarios
594 increased ET and decreased runoff, but created surprising, opposing trends in terms of changes in
595 deep drainage and seasonal water balances. These subtle differences carried over into daily and
596 seasonal energy balances, where the effects of increased ET and subsequent reduction in H did not
597 align across scenarios. Furthermore, while Downspout Disconnection increased runoff from
598 vegetated areas, this increase was less than the amount of runoff that would have been generated
599 from the rooftops, highlighting the complex interactions among diverse physical processes in cities
600 (Miles & Band, 2015). Our results align with other recent studies of urban tree effects based on

point simulations (Naika Meili et al., 2021), multi-layer turbulent closure of the integrated urban canopy with trees (Krayenhoff et al., 2020), and high-resolution urban hydrologic simulations (Arjenaki et al., 2021; Voter & Loheide, 2018), but with the added benefits of limited incurred computational cost and easy integration into regional climate and earth system simulations.

The interplay between rainfall characteristics and traditional hydrologic considerations, like antecedent soil moisture, are a key driver of variability among our simulations. While storm depth is inversely related to runoff reduction (Figure 2), it alone does not explain the variability seen across storms. "Second-order" rainfall characteristics are particularly important in urban regions due to the limited spatial scale of the regions themselves (Emmanuel et al., 2012) and highly connected impervious areas (Jacobson, 2011). Characteristics like time between storms can generate complex top layer soil conditions (Sun et al., 2018) that further change runoff generation and are especially important drivers of hydrologic heterogeneity at urban-vegetation interfaces (Yao et al., 2016). Timing between storms impacts not only the amount of ET and the duration of dry-down periods (Figure 5), but also the runoff generation mechanisms during subsequent storm (e.g., saturation excess vs. infiltration excess). It also influences the partitioning of energy into H and LE (Figure 7 and Figure 8), with drier conditions reducing ET due to soil water stress. ET rates within Urban Tree Expansion and Urban Tree Shift simulations are further linked to the "urban oasis effect," where ET from vegetation in urban areas—in this case over pavement—are large compared to similar vegetation in nonurban areas due to greater thermal loading and atmospheric demand brought about by less atmospheric water overall in urban areas (J. Yang et al., 2015; Ziter et al., 2019). When ET is reduced due to insufficient soil water, like in Urban Tree Shift, a reduction in H is still present due to radiative and thermal property changes, akin to behavior reported in other studies (Meili et al., 2021; Ryu et al., 2016; Schwaab et al., 2021; Zipper et al., 2017).

To develop distributions of new land-covers that are needed to run Noah-MP HUE, estimates of tree cover, buildings, and roadways are needed. One could use high resolution satellite remote sensing data, arial imagery like the National Agricultural Imagery Project (Earth Resources Observation And Science (EROS) Center, 2017), point clouds from LiDAR data, or publicly available geospatial layers from municipalities of interest. If using raw imagery/point cloud data, classification and segmentation would be needed to obtain estimates of tree cover (Bosch, 2020; L. Yang et al., 2009), buildings (Huang et al., 2022; Lu et al., 2014), and roadways (Liu et al., 2019). By overlaying the resulting tree cover and roadways, one could obtain a region's "Tree over Pavement." For Permeable Pavements, city ordinances and records can be used to estimate the location and amount of permeable pavement in an area, as well as an appropriate loading ratio. Finally, Downspout Disconnection could use open-source tax records to find buildings that are traditionally targeted for downspout disconnection initiatives (e.g., single family residences), and then either assume full disconnection (100%) or set a representative fraction in a region. Turfgrass, a key component of downspout disconnection, is not easily identified using the classification techniques mentioned above. Instead, an approach could be taken in which all other components of an urban area are accounted for using the above methods, and the remaining area is assumed to be turfgrass.

4.2 Implications for Urban Water and Heat Management Solutions

A key management takeaway from this study are that the specific placement of trees, impervious surface disconnections, and permeable pavements—often termed green infrastructure or nature-based solutions, but in reality, intrinsic features of the urban environment—can dramatically influence large scale hydrology. Careful consideration on the placement of many small-scale interventions can help reduce runoff generation "hotspots," though not every intervention may be appropriate for an area. For example, enhanced deep drainage may not be desired in a specific location due to potential negative effects including inundation of aging infrastructure (Peche et al., 2019), enhanced contaminant transport to groundwater (Andres et al., 2018), and "basement flooding" in areas with shallow or perched water tables.

Tree cover offers not only runoff reduction benefits (Selbig et al., 2022), but also co-benefits of temperature reduction that could be of service to cities' adaptation to climate warming. The initial placement of tree cover (i.e., Urban Tree Shift results) reduces runoff via interception. Runoff reduction will likely increase with tree age due to both a larger canopy enhancing interception and more root water uptake enhancing infiltration. At the same time, trees that overlap pavement provide shade, alter the albedo, emissivity, and other radiative properties (Naika Meili et al., 2021; Ziter et al., 2019). These changes can enhance ET and lower air temperatures in a wide range of climates (Schwaab et al., 2021), though in some cases, additional trees can enhance sensible heat and thus increase air temperatures due to changes in radiative properties increasing the absolute amount of energy available to be partitioned (Grimmond et al., 1996). Although urban trees provide a wide variety of ecosystem services, such as thermal comfort for humans (Sanusi et al., 2016), human health benefits (McDonald et al., 2016), reduced water pollution (Denman et al., 2016; Livesley, Ossola, et al., 2016), and even reduced urban air pollution (Livesley, McPherson, et al., 2016; Park & Schade, 2016), studies are needed to illuminate how urban transpiration rates vary across space and underlying climate and where trees can be placed to help reduce the effects of extreme heat (Winbourne et al., 2020). A way to involve community members in tree placement and to help avoid repeating past practices that have increased extreme heat exposure in marginalized communities, is through engagement programs like community-owned trees, solicitation of shade location priorities, and interviews to identify rain-induced runoff hotspots (Azizi et al., 2022; Guardaro et al., 2020; Hoffman et al., 2020; Wilson, 2020).

4.3 Limitations of this Study

Generally, we do not examine climate conditions associated with different regions in this study or parameter sensitivity (Cuntz et al. 2016). We examined a single soil texture class in this study—silt loam—using meteorology from three years at a single location (Milwaukee, Wisconsin) in a cool continental climate. Soil texture affects surface and subsurface processes in LSMs and regional climate simulations (Dennis & Berbery, 2021), especially for processes relating to surface runoff and ET. We provide examples of changes in results for Urban Tree Expansion and Urban Tree shift with a clay loam soil texture in Supplemental Information. Of note is that soil texture changes the amount of surface runoff and the percentage of tree canopy cover at which peak ET in Urban Tree Shift scenarios occurs. In addition, our study neglects other common aspects of urban soil, such as compaction due to lawn care, foot traffic, and construction equipment, which would increase surface runoff via reduction in topsoil porosity and hydraulic conductivity (Herrmann et al., 2017; Jian et al., 2021; Shuster et al., 2014; Voter & Loheide, 2018). Finally, our study does not consider the potential effects of groundwater. A high water table would

likely result in a reduced soil volume available for infiltration, as well as reduced infiltration capacity (Bhaskar et al., 2015).

Underlying climate also influences the effects of lateral transfers. Voter & Loheide (2021) examined the effects of downspout disconnection across the United States and found that runoff reduction partitioning between deep drainage and ET is strongly correlated with aridity index. Similarly, the type of urban vegetation and rates of ET vary with underlying climate (Mazrooei et al., 2021). Instead, our work presents an in-depth look at a single location to give insights into how fractional incrementation of the amount of lateral transfer changes the local water balance. Furthermore, we do not investigate differences brought about by strictly defining realistic representations of local or regional vegetation or landscaping, but instead use the concept of plant functional types. This approach is common in LSMs within earth system models (Duckworth et al., 2000).

Finally, our work only looks a small selection of low impact development practices (green infrastructure). While green infrastructure encompasses a wide variety of practices (Fletcher et al., 2015), the ones that we selected make up a majority of the regional green infrastructure plan within Milwaukee (Milwaukee Metropolitan Sewerage District, 2013). This work could be expanded to include modeling of other types green infrastructure practices, like bioretention swales and green roofs, but such measures may only make up a small fraction of an urban landscape.

5 Conclusions

While lateral transfers of water—and therefore of energy—are ubiquitous within complex urban environments and are increasingly recognized for the impact they have on water and energy cycles, they have been overlooked in land surface models (LSMs) to date. We present a new version of a widely-used LSM that integrates 1) land type mosaicking capabilities to address sub-grid heterogeneity in land cover/land use, and 2) the ability to transfer water between certain paired land types to better represent urban processes in a way that is usable and computationally efficient within coarse-scale regional climate and earth system models. We investigated the effects that incremental changes in the amount of lateral transfer have on both water and energy budgets. In terms of hydrologic impacts, disconnecting impervious surfaces and adding permeable pavement generated the largest decreases in runoff. There are more modest runoff benefits to adding tree canopy, as tree canopy overlying pavement causes interception and enhances infiltration due to increased drying of soils. The addition of trees that overhang pavements—a common feature in many real-world urban neighborhoods—offers the substantial co-benefit of increasing latent heat flux while decreasing the sensible heat flux. This would translate to reduced air temperatures. To our knowledge, these effects cannot be captured by other contemporary LSMs. The effects illustrated in this study are important due to implications for the potential regional feedbacks that urban water and energy fluxes have within the local and regional climate, as well as providing guidance for planners and communities seeking to reduce runoff and heat—important steps towards greater climate justice and equity in urban areas—through widespread but small-scale green infrastructure intervention.

Acknowledgements:
This work was supported by the Wisconsin Sea Grant, the Milwaukee Metropolitan Sewerage district, and the by the US Forest Service agreement #18-JV-11242308-016 under Focus Area 3

of the US EPA Great Lakes Restoration Initiative. We would like to acknowledge high-performance computing support from Cheyenne provided by NCAR's Computational and Information Systems Laboratory, sponsored by the National Science Foundation (Computational And Information Systems Laboratory, 2019) . We also would like to acknowledge Henrique Goulart and Holly Mallinson for comments on previous version of the manuscript. We also thank Dan Li for input on questions regarding implementation of the mosaicking scheme.

Data Availability Statement

NLDAS data for simulations is available for download through NASA's Goddard Earth Sciences data and Information Services Center (GES DISC) (https://disc.gsfc.nasa.gov/datasets?keywords=NLDAS). Noah-MP HUE, summary code data, and code used in the creation of this manuscript is available through a Zenodo repository (https://doi.org/10.5281/zenodo.8019119)

751 **Bibliography**
752
753 Alexander, G. A., Holmes, H. A., Sun, X., Caputi, D., Faloona, I. C., & Oldroyd, H. J. (2022).
754 Simulating land-atmosphere coupling in the Central Valley, California: Investigating soil
755 moisture impacts on boundary layer properties. *Agricultural and Forest Meteorology*,
756 *317*, 108898. https://doi.org/10.1016/j.agrformet.2022.108898
757 Andres, A. S., Ballestero, T. P., & Musick, M. L. (2018). Stormwater Management: When Is
758 Green Not So Green?: Stormwater Management: When Is Green Not So Green?
759 *Groundwater*, *56*(3), 357–358. https://doi.org/10.1111/gwat.12653
760 Arjenaki, M. O., Sanayei, H. R. Z., Heidarzadeh, H., & Mahabadi, N. A. (2021). Modeling and
761 investigating the effect of the LID methods on collection network of urban runoff using
762 the SWMM model (case study: Shahrekord City). *Modeling Earth Systems and*
763 *Environment*, *7*(1), 1–16. https://doi.org/10.1007/s40808-020-00870-2
764 Arsenault, K. R., Nearing, G. S., Wang, S., Yatheendradas, S., & Peters-Lidard, C. D. (2018).
765 Parameter Sensitivity of the Noah-MP Land Surface Model with Dynamic Vegetation.
766 *Journal of Hydrometeorology*, *19*(5), 815–830. https://doi.org/10.1175/jhm-d-17-0205.1
767 Avellaneda, P. M., Jefferson, A. J., Grieser, J. M., & Bush, S. A. (2017). Simulation of the
768 cumulative hydrological response to green infrastructure. *Water Resources Research*,
769 *53*(4), 3087–3101. https://doi.org/10.1002/2016WR019836
770 Azizi, K., Diko, S. K., Saija, L., Zamani, M. G., & Meier, C. I. (2022). Integrated community-
771 based approaches to urban pluvial flooding research, trends and future directions: A
772 review. *Urban Climate*, *44*, 101237. https://doi.org/10.1016/j.uclim.2022.101237
773 Barlage, M., Tewari, M., Chen, F., Miguez-Macho, G., Yang, Z.-L., & Niu, G.-Y. (2015). The
774 effect of groundwater interaction in North American regional climate simulations with

775 WRF/Noah-MP. *Climatic Change*, *129*(3–4), 485–498. https://doi.org/10.1007/s10584-
776 014-1308-8
777 Barlage, M., Chen, F., Rasmussen, R., Zhang, Z., & Miguez-Macho, G. (2021). The Importance
778 of Scale-Dependent Groundwater Processes in Land-Atmosphere Interactions Over the
779 Central United States. *Geophysical Research Letters*, *48*(5).
780 https://doi.org/10.1029/2020GL092171
781 Berg, A., Lintner, B. R., Findell, K. L., Malyshev, S., Loikith, P. C., & Gentine, P. (2014).
782 Impact of Soil Moisture–Atmosphere Interactions on Surface Temperature Distribution.
783 *Journal of Climate*, *27*(21), 7976–7993. https://doi.org/10.1175/JCLI-D-13-00591.1
784 Best, M. J., Pryor, M., Clark, D. B., Rooney, G. G., Essery, R. . L. H., Ménard, C. B., et al.
785 (2011). The Joint UK Land Environment Simulator (JULES), model description – Part 1:
786 Energy and water fluxes. *Geoscientific Model Development*, *4*(3), 677–699.
787 https://doi.org/10.5194/gmd-4-677-2011
788 Bhaskar, A. S., Welty, C., Maxwell, R. M., & Miller, A. J. (2015). Untangling the effects of
789 urban development on subsurface storage in Baltimore. *Water Resources Research*,
790 *51*(2), 1158–1181. https://doi.org/10.1002/2014WR016039
791 Bosch, M. (2020). DetecTree: Tree detection from aerial imagery in Python. *Journal of Open*
792 *Source Software*, *5*(50), 2172. https://doi.org/10.21105/joss.02172
793 Brutsaert, W. (1982). *Evaporation into the Atmosphere*. Dordrecht: Springer Netherlands.
794 https://doi.org/10.1007/978-94-017-1497-6
795 Cai, X., Yang, Z.-L., David, C. H., Niu, G.-Y., & Rodell, M. (2014). Hydrological evaluation of
796 the Noah-MP land surface model for the Mississippi River Basin: HYDROLOGICAL

EVALUATION OF NOAH-MP. *Journal of Geophysical Research: Atmospheres*, *119*(1), 23–38. https://doi.org/10.1002/2013JD020792

Chen, F., & Zonato, A. (2021). *Updates of WRF-urban in WRF 4.3: Local Climate Zones, Mitigation Strategies, building materials permeability and new buildings drag coefficient* (p. 5). RAL. Retrieved from https://ral.ucar.edu/sites/default/files/public/product-tool/urban-canopy-model/WRF_urban_update_Readme_file_WRF4.3.pdf

Chen, F., Mitchell, K., Schaake, J., Xue, Y., Pan, H.-L., Koren, V., et al. (1996). Modeling of land surface evaporation by four schemes and comparison with FIFE observations. *Journal of Geophysical Research: Atmospheres*, *101*(D3), 7251–7268. https://doi.org/10.1029/95JD02165

Chen, F., Kusaka, H., Bornstein, R., Ching, J., Grimmond, C. S. B., Grossman-Clarke, S., et al. (2011). The integrated WRF/urban modelling system: development, evaluation, and applications to urban environmental problems. *International Journal of Climatology*, *31*(2), 273–288. https://doi.org/10.1002/joc.2158

Computational And Information Systems Laboratory. (2019). Cheyenne: SGI ICE XA Cluster. https://doi.org/10.5065/D6RX99HX

Cuntz, M., Mai, J., Samaniego, L., Clark, M., Wulfmeyer, V., Branch, O., et al. (2016). The impact of standard and hard-coded parameters on the hydrologic fluxes in the Noah-MP land surface model: HARD-CODED PARAMETERS IN NOAH-MP. *Journal of Geophysical Research: Atmospheres*, *121*(18), 10,676-10,700. https://doi.org/10.1002/2016JD025097

818 Denman, E. C., May, P. B., & Moore, G. M. (2016). The Potential Role of Urban Forests in
819 Removing Nutrients from Stormwater. *Journal of Environmental Quality*, *45*(1), 207–
820 214. https://doi.org/10.2134/jeq2015.01.0047
821 Dennis, E. J., & Berbery, E. H. (2021). The Role of Soil Texture in Local Land Surface–
822 Atmosphere Coupling and Regional Climate. *Journal of Hydrometeorology*, *22*(2), 313–
823 330. https://doi.org/10.1175/JHM-D-20-0047.1
824 Department of Energy & Environment, G. of the D. of C. (2019). Stormwater Guidebook:
825 Permeable Pavement Systems. Retrieved from 1
826 https://doee.dc.gov/sites/default/files/dc/sites/ddoe/page_content/attachments/Stormwater
827 %20Guidebook_Permeable%20Pavement%20Systems.pdf
828 Department of Environmental Quality, N. C. (2020, November 20). Stormwater Design Manual:
829 C-5. Permeable Pavement. Retrieved from https://www.deq.nc.gov/energy-mineral-and-
830 land-resources/stormwater/bmp-manual/c-5-permeable-pavement-11-20-2020/download
831 Department of Natural Resources, W. (2021). WISCONSIN DEPARTMENT OF NATURAL
832 RESOURCES TECHNICAL STANDARD PERMEABLE PAVEMENT. Retrieved from
833 https://dnr.wisconsin.gov/sites/default/files/topic/Stormwater/1008_PermeablePavement_
834 06-2021.pdf
835 Dewitz, J. (2021). National Land Cover Database (NLCD) 2019 Products [Data set]. U.S.
836 Geological Survey. https://doi.org/10.5066/P9KZCM54
837 Duckworth, J. C., Kent, M., & Ramsay, P. M. (2000). Plant functional types: an alternative to
838 taxonomic plant community description in biogeography? *Progress in Physical*
839 *Geography: Earth and Environment*, *24*(4), 515–542.
840 https://doi.org/10.1177/030913330002400403

841 Earth Resources Observation And Science (EROS) Center. (2017). National Agriculture Imagery
842 Program (NAIP) [Tiff]. U.S. Geological Survey. https://doi.org/10.5066/F7QN651G
843 Ek, M. B., Mitchell, K. E., Lin, Y., Rogers, E., Grunmann, P., Koren, V., et al. (2003).
844 Implementation of Noah land surface model advances in the National Centers for
845 Environmental Prediction operational mesoscale Eta model. *Journal of Geophysical*
846 *Research: Atmospheres*, *108*(D22), 2002JD003296.
847 https://doi.org/10.1029/2002JD003296
848 Emmanuel, I., Andrieu, H., Leblois, E., & Flahaut, B. (2012). Temporal and spatial variability of
849 rainfall at the urban hydrological scale. *Journal of Hydrology*, *430–431*, 162–172.
850 https://doi.org/10.1016/j.jhydrol.2012.02.013
851 Essery, R. L. H., Best, M. J., Betts, R. A., Cox, P. M., & Taylor, C. M. (2003). Explicit
852 Representation of Subgrid Heterogeneity in a GCM Land Surface Scheme. *Journal of*
853 *Hydrometeorology*, *4*(3), 530–543. https://doi.org/10.1175/1525-
854 7541(2003)004<0530:EROSHI>2.0.CO;2
855 Feddes, R. A., Kowalik, P., Kolinska-Malinka, K., & Zaradny, H. (1976). Simulation of field
856 water uptake by plants using a soil water dependent root extraction function. *Journal of*
857 *Hydrology*, *31*(1–2), 13–26. https://doi.org/10.1016/0022-1694(76)90017-2
858 Fisher, R. A., & Koven, C. D. (2020). Perspectives on the Future of Land Surface Models and
859 the Challenges of Representing Complex Terrestrial Systems. *Journal of Advances in*
860 *Modeling Earth Systems*, *12*(4). https://doi.org/10.1029/2018MS001453
861 Fletcher, T. D., Shuster, W., Hunt, W. F., Ashley, R., Butler, D., Arthur, S., et al. (2015). SUDS,
862 LID, BMPs, WSUD and more – The evolution and application of terminology

surrounding urban drainage. *Urban Water Journal*, *12*(7), 525–542. https://doi.org/10.1080/1573062X.2014.916314

Fung, K. Y., Yang, Z.-L., & Niyogi, D. (2022). Improving the local climate zone classification with building height, imperviousness, and machine learning for urban models. *Computational Urban Science*, *2*(1), 16. https://doi.org/10.1007/s43762-022-00046-x

Gale, M. R., & Grigal, D. F. (1987). Vertical root distributions of northern tree species in relation to successional status. *Canadian Journal of Forest Research*, *17*(8), 829–834. https://doi.org/10.1139/x87-131

Gochis, D., Barlage, M., Dugger, A., FitzGerald, K., Karsten, L., McAllister, M., et al. (2018). WRF-Hydro Model Source Code Version 5 [Fortran90]. UCAR/NCAR. https://doi.org/10.5065/D6J38RBJ

Grimmond, C., Souch, C., & Hubble, M. (1996). Influence of tree cover on summertime surface energy balance fluxes, San Gabriel Valley, Los Angeles. *Climate Research*, *6*, 45–57. https://doi.org/10.3354/cr006045

Grimmond, C. S. B., & Oke, T. R. (2002). Turbulent Heat Fluxes in Urban Areas: Observations and a Local-Scale Urban Meteorological Parameterization Scheme (LUMPS). *Journal of Applied Meteorology*, *41*(7), 792–810. https://doi.org/10.1175/1520-0450(2002)041<0792:THFIUA>2.0.CO;2

Guardaro, M., Messerschmidt, M., Hondula, D. M., Grimm, N. B., & Redman, C. L. (2020). Building community heat action plans story by story: A three neighborhood case study. *Cities*, *107*, 102886. https://doi.org/10.1016/j.cities.2020.102886

He, C., Chen, F., Abolafia-Rosenzweig, R., Ikeda, K., Liu, C., & Rasmussen, R. (2021). What Causes the Unobserved Early-Spring Snowpack Ablation in Convection-Permitting WRF

886 Modeling Over Utah Mountains? *Journal of Geophysical Research: Atmospheres*,
887 *126*(22), e2021JD035284. https://doi.org/10.1029/2021JD035284
888 He, C., Valayamkunnath, P., Barlage, M., Chen, F., Gochis, D., Cabell, R., et al. (2023). *The*
889 *Community Noah-MP Land Surface Modeling System Technical Description Version 5.0*.
890 NCAR/UCAR. https://doi.org/10.5065/EW8G-YR95
891 Herrmann, D. L., Shuster, W. D., & Garmestani, A. S. (2017). Vacant urban lot soils and their
892 potential to support ecosystem services. *Plant and Soil*, *413*(1–2), 45–57.
893 https://doi.org/10.1007/s11104-016-2874-5
894 Hoffman, J. S., Shandas, V., & Pendleton, N. (2020). The Effects of Historical Housing Policies
895 on Resident Exposure to Intra-Urban Heat: A Study of 108 US Urban Areas. *Climate*,
896 *8*(1), 12. https://doi.org/10.3390/cli8010012
897 Hollis, G. E. (1975). The effect of urbanization on floods of different recurrence interval. *Water*
898 *Resources Research*, *11*(3), 431–435. https://doi.org/10.1029/WR011i003p00431
899 Huang, X., Ren, L., Liu, C., Wang, Y., Yu, H., Schmitt, M., et al. (2022). Urban Building
900 Classification (UBC) – A Dataset for Individual Building Detection and Classification
901 from Satellite Imagery. In *2022 IEEE/CVF Conference on Computer Vision and Pattern*
902 *Recognition Workshops (CVPRW)* (pp. 1412–1420). New Orleans, LA, USA: IEEE.
903 https://doi.org/10.1109/CVPRW56347.2022.00147
904 Jacobson, C. R. (2011). Identification and quantification of the hydrological impacts of
905 imperviousness in urban catchments: A review. *Journal of Environmental Management*,
906 *92*(6), 1438–1448. https://doi.org/10.1016/j.jenvman.2011.01.018

907 Jian, J., Shiklomanov, A., Shuster, W. D., & Stewart, R. D. (2021). Predicting near-saturated
908 hydraulic conductivity in urban soils. *Journal of Hydrology*, *595*, 126051.
909 https://doi.org/10.1016/j.jhydrol.2021.126051
910 Jordan, R. E. (1991). A One-dimensional temperature model for a snow cover : technical
911 documentation for SNTHERM.89. *This Digital Resource Was Created from Scans of the*
912 *Print Resource*. Retrieved from https://erdc-
913 library.erdc.dren.mil/jspui/handle/11681/11677
914 Koster, R. D., Dirmeyer, P. A., Guo, Z., Bonan, G., Chan, E., Cox, P., et al. (2004). Regions of
915 Strong Coupling Between Soil Moisture and Precipitation. *Science*, *305*(5687), 1138–
916 1140. https://doi.org/10.1126/science.1100217
917 Krayenhoff, E. S., Jiang, T., Christen, A., Martilli, A., Oke, T. R., Bailey, B. N., et al. (2020). A
918 multi-layer urban canopy meteorological model with trees (BEP-Tree): Street tree
919 impacts on pedestrian-level climate. *Urban Climate*, *32*, 100590.
920 https://doi.org/10.1016/j.uclim.2020.100590
921 Kusaka, H., Kondo, H., Kikegawa, Y., & Kimura, F. (2001). A Simple Single-Layer Urban
922 Canopy Model For Atmospheric Models: Comparison With Multi-Layer And Slab
923 Models. *Boundary-Layer Meteorology*, *101*(3), 329–358.
924 https://doi.org/10.1023/A:1019207923078
925 Leopold, L. B. (1968). *Hydrology for urban land planning - A guidebook on the hydrologic*
926 *effects of urban land use* (Report No. 554) (p. 26). Reston, VA.
927 https://doi.org/10.3133/cir554

928 Li, D., Bou-Zeid, E., Barlage, M., Chen, F., & Smith, J. A. (2013). Development and evaluation
929 of a mosaic approach in the WRF-Noah framework. *Journal of Geophysical Research*
930 *Atmospheres*, *118*(21), 11,918-11,935. https://doi.org/10.1002/2013JD020657
931 Lin, P., Hopper, L. J., Yang, Z.-L., Lenz, M., & Zeitler, J. W. (2018). Insights into
932 Hydrometeorological Factors Constraining Flood Prediction Skill during the May and
933 October 2015 Texas Hill Country Flood Events. *Journal of Hydrometeorology*, *19*(8),
934 1339–1361. https://doi.org/10.1175/JHM-D-18-0038.1
935 Liu, Y., Yao, J., Lu, X., Xia, M., Wang, X., & Liu, Y. (2019). RoadNet: Learning to
936 Comprehensively Analyze Road Networks in Complex Urban Scenes From High-
937 Resolution Remotely Sensed Images. *IEEE Transactions on Geoscience and Remote*
938 *Sensing*, *57*(4), 2043–2056. https://doi.org/10.1109/TGRS.2018.2870871
939 Livesley, S. J., Ossola, A., Threlfall, C. G., Hahs, A. K., & Williams, N. S. G. (2016). Soil
940 Carbon and Carbon/Nitrogen Ratio Change under Tree Canopy, Tall Grass, and Turf
941 Grass Areas of Urban Green Space. *Journal of Environmental Quality*, *45*(1), 215–223.
942 https://doi.org/10.2134/jeq2015.03.0121
943 Livesley, S. J., McPherson, E. G., & Calfapietra, C. (2016). The Urban Forest and Ecosystem
944 Services: Impacts on Urban Water, Heat, and Pollution Cycles at the Tree, Street, and
945 City Scale. *Journal of Environmental Quality*, *45*(1), 119–124.
946 https://doi.org/10.2134/jeq2015.11.0567
947 Lorenz, R., Argüeso, D., Donat, M. G., Pitman, A. J., Hurk, B., Berg, A., et al. (2016). Influence
948 of land-atmosphere feedbacks on temperature and precipitation extremes in the GLACE-
949 CMIP5 ensemble. *Journal of Geophysical Research: Atmospheres*, *121*(2), 607–623.
950 https://doi.org/10.1002/2015JD024053

951 Lu, Z., Im, J., Rhee, J., & Hodgson, M. (2014). Building type classification using spatial and
952 landscape attributes derived from LiDAR remote sensing data. *Landscape and Urban*
953 *Planning*, *130*, 134–148. https://doi.org/10.1016/j.landurbplan.2014.07.005
954 Ma, N., Niu, G.-Y., Xia, Y., Cai, X., Zhang, Y., Ma, Y., & Fang, Y. (2017). A Systematic
955 Evaluation of Noah-MP in Simulating Land-Atmosphere Energy, Water, and Carbon
956 Exchanges Over the Continental United States: Noah-MP Evaluation in CONUS. *Journal*
957 *of Geophysical Research: Atmospheres*, *122*(22), 12,245-12,268.
958 https://doi.org/10.1002/2017JD027597
959 Marando, F., Heris, M. P., Zulian, G., Udías, A., Mentaschi, L., Chrysoulakis, N., et al. (2022).
960 Urban heat island mitigation by green infrastructure in European Functional Urban Areas.
961 *Sustainable Cities and Society*, *77*, 103564. https://doi.org/10.1016/j.scs.2021.103564
962 Martilli, A., Clappier, A., & Rotach, M. W. (2002). An Urban Surface Exchange
963 Parameterisation for Mesoscale Models. *Boundary-Layer Meteorology*, *104*(2), 261–304.
964 https://doi.org/10.1023/A:1016099921195
965 Mazrooei, A., Reitz, M., Wang, D., & Sankarasubramanian, A. (2021). Urbanization Impacts on
966 Evapotranspiration Across Various Spatio-Temporal Scales. *Earth's Future*, *9*(8).
967 https://doi.org/10.1029/2021EF002045
968 McDonald, R., Kroeger, T., Boucher, T., Wang, L., Salem, R., & others. (2016). Planting healthy
969 air: a global analysis of the role of urban trees in addressing particulate matter pollution
970 and extreme heat. *Planting Healthy Air: A Global Analysis of the Role of Urban Trees in*
971 *Addressing Particulate Matter Pollution and Extreme Heat.*
972 Meili, N., Manoli, G., Burlando, P., Bou-Zeid, E., Chow, W. T. L., Coutts, A. M., et al. (2020).
973 An urban ecohydrological model to quantify the effect of vegetation on urban climate and

974 hydrology (UT&C v1.0). *Geosci. Model Dev.*, *13*(1), 335–362.
975 https://doi.org/10.5194/gmd-13-335-2020
976 Meili, Naika, Manoli, G., Burlando, P., Carmeliet, J., Chow, W. T. L., Coutts, A. M., et al.
977 (2021). Tree effects on urban microclimate: Diurnal, seasonal, and climatic temperature
978 differences explained by separating radiation, evapotranspiration, and roughness effects.
979 *Urban Forestry & Urban Greening*, *58*, 126970.
980 https://doi.org/10.1016/j.ufug.2020.126970
981 Miles, B., & Band, L. E. (2015). Green infrastructure stormwater management at the watershed
982 scale: urban variable source area and watershed capacitance: INVITED
983 COMMENTARY. *Hydrological Processes*, *29*(9), 2268–2274.
984 https://doi.org/10.1002/hyp.10448
985 Miller, D. L., Alonzo, M., Roberts, D. A., Tague, C. L., & McFadden, J. P. (2020). Drought
986 response of urban trees and turfgrass using airborne imaging spectroscopy. *Remote*
987 *Sensing of Environment*, *240*, 111646. https://doi.org/10.1016/j.rse.2020.111646
988 Milwaukee Metropolitan Sewerage District. (2013). *MMSD Regional Green Infrastructure Plan*.
989 Miralles, D. G., Gentine, P., Seneviratne, S. I., & Teuling, A. J. (2019). Land-atmospheric
990 feedbacks during droughts and heatwaves: state of the science and current challenges:
991 Land feedbacks during droughts and heatwaves. *Annals of the New York Academy of*
992 *Sciences*, *1436*(1), 19–35. https://doi.org/10.1111/nyas.13912
993 Mu, Q., Miao, S., Wang, Y., Li, Y., He, X., & Yan, C. (2020). Evaluation of employing local
994 climate zone classification for mesoscale modelling over Beijing metropolitan area.
995 *Meteorology and Atmospheric Physics*, *132*(3), 315–326. https://doi.org/10.1007/s00703-
996 019-00692-7

997 Niu, G. Y., Yang, Z. L., Mitchell, K. E., Chen, F., Ek, M. B., Barlage, M., et al. (2011). The
998 community Noah land surface model with multiparameterization options (Noah-MP): 1.
999 Model description and evaluation with local-scale measurements. *Journal of Geophysical*
1000 *Research Atmospheres*, *116*(D12). https://doi.org/10.1029/2010JD015139
1001 Niu, G.-Y., & Yang, Z.-L. (2006). Effects of Frozen Soil on Snowmelt Runoff and Soil Water
1002 Storage at a Continental Scale. *Journal of Hydrometeorology*, *7*(5), 937–952.
1003 https://doi.org/10.1175/JHM538.1
1004 Oke, T. R., Mills, G. M., Christen, A., & Voogt, J. A. (2017). *Urban climates*. Cambridge,
1005 United Kingdom: Cambridge University Press.
1006 Oleson, K., Lawrence, M., Bonan, B., Drewniak, B., Huang, M., Koven, D., et al. (2013).
1007 Technical description of version 4.5 of the Community Land Model (CLM).
1008 https://doi.org/10.5065/D6RR1W7M
1009 Oleson, K. W., Bonan, G. B., Feddema, J., Vertenstein, M., & Grimmond, C. S. B. (2008). An
1010 Urban Parameterization for a Global Climate Model. Part I: Formulation and Evaluation
1011 for Two Cities. *Journal of Applied Meteorology and Climatology*, *47*(4), 1038–1060.
1012 https://doi.org/10.1175/2007JAMC1597.1
1013 Park, C., & Schade, G. W. (2016). Anthropogenic and Biogenic Features of Long-Term
1014 Measured CO2 Flux in North Downtown Houston, Texas. *Journal of Environmental*
1015 *Quality*, *45*(1), 253–265. https://doi.org/10.2134/jeq2015.02.0115
1016 Peche, A., Graf, T., Fuchs, L., & Neuweiler, I. (2019). Physically based modeling of stormwater
1017 pipe leakage in an urban catchment. *Journal of Hydrology*, *573*, 778–793.
1018 https://doi.org/10.1016/j.jhydrol.2019.03.016

1019 Pollution Control Agency, M. (2022, December 29). Minnesota Stormwater Manual: Design
1020 criteria for permeable pavement. Retrieved from
1021 https://stormwater.pca.state.mn.us/index.php/Design_criteria_for_permeable_pavement
1022 Ribeiro, I., Martilli, A., Falls, M., Zonato, A., & Villalba, G. (2021). Highly resolved WRF-
1023 BEP/BEM simulations over Barcelona urban area with LCZ. *Atmospheric Research*, *248*,
1024 105220. https://doi.org/10.1016/j.atmosres.2020.105220
1025 Ryu, Y. H., Bou-Zeid, E., Wang, Z. H., & Smith, J. A. (2016). Realistic Representation of Trees
1026 in an Urban Canopy Model. *Boundary-Layer Meteorology*, *159*(2), 193–220.
1027 https://doi.org/10.1007/s10546-015-0120-y
1028 Sakaguchi, K., & Zeng, X. (2009). Effects of soil wetness, plant litter, and under-canopy
1029 atmospheric stability on ground evaporation in the Community Land Model (CLM3.5):
1030 NEW SCHEMES FOR CLM3.5 SOIL EVAPORATION. *Journal of Geophysical*
1031 *Research: Atmospheres*, *114*(D1). https://doi.org/10.1029/2008JD010834
1032 Sanusi, R., Johnstone, D., May, P., & Livesley, S. J. (2016). Street Orientation and Side of the
1033 Street Greatly Influence the Microclimatic Benefits Street Trees Can Provide in Summer.
1034 *Journal of Environmental Quality*, *45*(1), 167–174.
1035 https://doi.org/10.2134/jeq2015.01.0039
1036 Schaake, J. C., Koren, V. I., Duan, Q., Mitchell, K., & Chen, F. (1996). Simple water balance
1037 model for estimating runoff at different spatial and temporal scales. *Journal of*
1038 *Geophysical Research: Atmospheres*, *101*(D3), 7461–7475.
1039 https://doi.org/10.1029/95JD02892

1040 Schwaab, J., Meier, R., Mussetti, G., Seneviratne, S., Bürgi, C., & Davin, E. L. (2021a). The role
1041 of urban trees in reducing land surface temperatures in European cities. *Nature*
1042 *Communications*, *12*(1), 6763. https://doi.org/10.1038/s41467-021-26768-w
1043 Schwaab, J., Meier, R., Mussetti, G., Seneviratne, S., Bürgi, C., & Davin, E. L. (2021b). The role
1044 of urban trees in reducing land surface temperatures in European cities. *Nature*
1045 *Communications*, *12*(1), 1–11. https://doi.org/10.1038/s41467-021-26768-w
1046 Selbig, W. R., Loheide, S. P., Shuster, W., Scharenbroch, B. C., Coville, R. C., Kruegler, J., et al.
1047 (2022). Quantifying the stormwater runoff volume reduction benefits of urban street tree
1048 canopy. *Science of the Total Environment*, *806*, 151296.
1049 https://doi.org/10.1016/j.scitotenv.2021.151296
1050 Sharma, A., Wuebbles, D. J., & Kotamarthi, R. (2021). The Need for Urban-Resolving Climate
1051 Modeling Across Scales. *AGU Advances*, *2*(1). https://doi.org/10.1029/2020AV000271
1052 Shields, C., & Tague, C. (2015). Ecohydrology in semiarid urban ecosystems: Modeling the
1053 relationship between connected impervious area and ecosystem productivity. *Water*
1054 *Resources Research*, *51*(1), 302–319. https://doi.org/10.1002/2014WR016108
1055 Shuster, W. D., Dadio, S., Drohan, P., Losco, R., & Shaffer, J. (2014). Residential demolition
1056 and its impact on vacant lot hydrology: Implications for the management of stormwater
1057 and sewer system overflows. *Landscape and Urban Planning*, *125*, 48–56.
1058 https://doi.org/10.1016/j.landurbplan.2014.02.003
1059 Skamarock, W. C., Klemp, J. B., Dudhia, J., Gill, D. O., Liu, Z., Berner, J., et al. (2019). *A*
1060 *Description of the Advanced Research WRF Model Version 4*. UCAR/NCAR.
1061 https://doi.org/10.5065/1DFH-6P97

1062 Sun, A. Y., Xia, Y., Caldwell, T. G., & Hao, Z. (2018). Patterns of precipitation and soil
1063 moisture extremes in Texas, US: A complex network analysis. *Advances in Water*
1064 *Resources*, *112*, 203–213. https://doi.org/10.1016/j.advwatres.2017.12.019
1065 Sun, X., Holmes, H., Osibanjo, O., Sun, Y., & Ivey, C. (2017). Evaluation of Surface Fluxes in
1066 the WRF Model: Case Study for Farmland in Rolling Terrain. *Atmosphere*, *8*(12), 197.
1067 https://doi.org/10.3390/atmos8100197
1068 Vahmani, P., & Hogue, T. S. (2015). Urban irrigation effects on WRF-UCM summertime
1069 forecast skill over the Los Angeles metropolitan area. *Journal of Geophysical Research:*
1070 *Atmospheres*, *120*(19), 9869–9881. https://doi.org/10.1002/2015JD023239
1071 Verseghy, D. L. (2007). Class-A Canadian land surface scheme for GCMS. I. Soil model.
1072 *International Journal of Climatology*, *11*(2), 111–133.
1073 https://doi.org/10.1002/joc.3370110202
1074 Vogel, M. M., Orth, R., Cheruy, F., Hagemann, S., Lorenz, R., Hurk, B. J. J. M., & Seneviratne,
1075 S. I. (2017). Regional amplification of projected changes in extreme temperatures
1076 strongly controlled by soil moisture-temperature feedbacks. *Geophysical Research*
1077 *Letters*, *44*(3), 1511–1519. https://doi.org/10.1002/2016GL071235
1078 Voter, C. B., & Loheide, S. P. (2018). Urban Residential Surface and Subsurface Hydrology:
1079 Synergistic Effects of Low-Impact Features at the Parcel Scale. *Water Resources*
1080 *Research*, *54*(10), 8216–8233. https://doi.org/10.1029/2018WR022534
1081 Voter, Carolyn B, & Loheide, S. P. (2021). Climatic controls on the hydrologic effects of urban
1082 low impact development practices. *Environmental Research Letters*, *16*(6), 064021.
1083 https://doi.org/10.1088/1748-9326/abfc06

1084 Wakefield, R. A., Basara, J. B., Shepherd, J. M., Brauer, N., Furtado, J. C., Santanello, J. A., &
1085 Edwards, R. (2021). The Inland Maintenance and Reintensification of Tropical Storm
1086 Bill (2015) Part 1: Contributions of the Brown Ocean Effect. *Journal of*
1087 *Hydrometeorology*. https://doi.org/10.1175/JHM-D-20-0150.1
1088 Walsh, C. J., Roy, A. H., Feminella, J. W., Cottingham, P. D., Groffman, P. M., & Morgan, R. P.
1089 (2005). The urban stream syndrome: current knowledge and the search for a cure.
1090 *Journal of the North American Benthological Society*, *24*(3), 706–723.
1091 https://doi.org/10.1899/04-028.1
1092 Wang, Y., Zhang, X., Xu, J., Pan, G., Zhao, Y., Liu, Y., et al. (2022). Accumulated impacts of
1093 imperviousness on surface and subsurface hydrology—continuous modelling at urban
1094 street block scale. *Journal of Hydrology*, *608*, 127621.
1095 https://doi.org/10.1016/j.jhydrol.2022.127621
1096 Welty, J., Stillman, S., Zeng, X., & Santanello, J. (2020). Increased Likelihood of Appreciable
1097 Afternoon Rainfall Over Wetter or Drier Soils Dependent Upon Atmospheric Dynamic
1098 Influence. *Geophysical Research Letters*, *47*(11), 1–9.
1099 https://doi.org/10.1029/2020GL087779
1100 Wilson, B. (2020). Urban Heat Management and the Legacy of Redlining. *Journal of the*
1101 *American Planning Association*, *86*(4), 443–457.
1102 https://doi.org/10.1080/01944363.2020.1759127
1103 Winbourne, J. B., Jones, T. S., Garvey, S. M., Harrison, J. L., Wang, L., Li, D., et al. (2020).
1104 Tree Transpiration and Urban Temperatures: Current Understanding, Implications, and
1105 Future Research Directions. *BioScience*, *70*(7), 576–588.
1106 https://doi.org/10.1093/biosci/biaa055

1107 Wright, D. B., Smith, J. A., Villarini, G., & Baeck, M. L. (2012). Hydroclimatology of flash
1108 flooding in Atlanta: THE HYDROCLIMATOLOGY OF FLASH FLOODING IN
1109 ATLANTA. *Water Resources Research*, *48*(4). https://doi.org/10.1029/2011WR011371
1110 Yang, J., Wang, Z. H., Chen, F., Miao, S., Tewari, M., Voogt, J. A., & Myint, S. (2015).
1111 Enhancing Hydrologic Modelling in the Coupled Weather Research and Forecasting–
1112 Urban Modelling System. *Boundary-Layer Meteorology*, *155*(1), 87–109.
1113 https://doi.org/10.1007/s10546-014-9991-6
1114 Yang, L., Wu, X., Praun, E., & Ma, X. (2009). Tree detection from aerial imagery. In
1115 *Proceedings of the 17th ACM SIGSPATIAL International Conference on Advances in*
1116 *Geographic Information Systems* (pp. 131–137). New York, NY, USA: Association for
1117 Computing Machinery. https://doi.org/10.1145/1653771.1653792
1118 Yao, L., Wei, W., & Chen, L. (2016). How does imperviousness impact the urban rainfall-runoff
1119 process under various storm cases? *Ecological Indicators*, *60*, 893–905.
1120 https://doi.org/10.1016/j.ecolind.2015.08.041
1121 Zeng, X. (2001). Global Vegetation Root Distribution for Land Modeling. *Journal of*
1122 *Hydrometeorology*, *2*(5), 525–530. https://doi.org/10.1175/1525-
1123 7541(2001)002<0525:GVRDFL>2.0.CO;2
1124 Zipper, S. C., Schatz, J., Kucharik, C. J., & Loheide, S. P. (2017). Urban heat island-induced
1125 increases in evapotranspirative demand. *Geophysical Research Letters*, *44*(2), 873–881.
1126 https://doi.org/10.1002/2016GL072190
1127 Ziter, C. D., Pedersen, E. J., Kucharik, C. J., & Turner, M. G. (2019). Scale-dependent
1128 interactions between tree canopy cover and impervious surfaces reduce daytime urban

heat during summer. *Proceedings of the National Academy of Sciences*, *116*(15), 7575–7580. https://doi.org/10.1073/pnas.1817561116